



Full length article

Surface chemistry and morphology transition induced by critical heat flux incipience on laser-textured copper surfaces

Matic Može^{a,*}, Matevž Zupančič^a, Matej Hočevar^b, Iztok Golobič^a, Peter Gregorčič^{a,*}^a Faculty of Mechanical Engineering, University of Ljubljana, Aškerčeva 6, 1000 Ljubljana, Slovenia^b Institute of Metals and Technology, Lepi pot 11, 1000 Ljubljana, Slovenia

ARTICLE INFO

Keywords:

Functionalized surfaces
Laser surface engineering
Laser texturing
Laser ablation
Heat transfer
Nucleate boiling

ABSTRACT

Stability of functionalized surfaces is an often-neglected topic in phase-change heat transfer research. Here, we examine the chemical and morphological changes of textured surfaces on the molecular and atomic level after the critical heat flux incipience during saturated pool-boiling of water. SEM imaging, EDS, AES and XPS analyses are used to examine the surface changes. Copper samples were laser textured via ablation using a nanosecond fiber laser under air or argon atmosphere. Multiscale microcavities, which serve as preferential nucleation sites, were produced on the samples, which exhibited significantly enhanced heat transfer performance in pool-boiling tests. Repeated formation of a vapor film and accompanying temperatures of up to 320 °C during the tests resulted in changes of the surface chemistry and nanomorphology. It was determined that Cu (II) oxide and hydroxide transform into Cu (I) oxide and Cu metal as a result of repeated low-temperature annealing of the surface when a vapor film is formed during the transition towards film boiling. This additionally causes a wettability transition of the functionalized surfaces from hydrophilic towards hydrophobic. Both effects importantly influence the solid-liquid-vapor interface during phase-change heat transfer. Overall, surfaces functionalized via laser texturing exhibited significantly enhanced stability and boiling heat transfer performance.

1. Introduction

Boiling is one of the most efficient mechanism of heat transfer in high heat flux applications, such as nuclear reactors, (micro)electronic components and supercomputer cooling. This is due to extremely high heat transfer coefficients (HTC) that allow small surface superheats at high heat fluxes. Here, the surface superheat is defined as the excess temperature of the surface relative to the temperature of the working fluid. The typical boiling curve [1], i.e., the heat flux as a function of the surface superheat, is shown in Fig. 1. As the surface superheat increases, the boiling process progresses from natural convection to film boiling. The transition from the desired nucleate boiling into undesirable film boiling happens at the upper heat flux limit, defined as the critical heat flux (CHF). For water at atmospheric pressure, this typically transpires at around 1 MW m^{-2} .

Boiling heat transfer involves intense processes including the vaporization of the working fluid, high surface temperatures and high-frequency temperature variations due to bubble nucleation. These phenomena interact with the boiling surface in such extent that they can change its physical and chemical properties over time. While long-term effects on the boiling heat transfer parameters have been

investigated in the past [2,3], there are practically no publications discussing specific changes of the surface either after prolonged exposure to boiling or after the first incipience of the CHF and the subsequent transition into film boiling. Furthermore, it is still not well understood how the surface chemistry and morphology of functionalized (e.g. in similar way as in Ref. [4]) surfaces are affected by the high temperatures that are invariably present within the transition and film boiling region. Finally, the boiling process affects the wettability of the surface in yet not fully understood ways. Changes in the chemical composition and morphology of the surface are the most likely causes for the wettability alterations.

Even though boiling heat transfer is, alongside with condensation, one of the most intensive convective heat transfer processes, it can still be improved. A multitude of factors affect the boiling process and heat transfer. These include the physical, thermodynamic and wetting properties of the working fluid and the environmental parameters (pressure, gravity, electromagnetic fields etc.). The most researched and prospective approach in boiling enhancement is the modification of the boiling surface and its interaction with the working fluid at the solid-liquid-vapor interface. Most research efforts are aimed at enhancing this interaction through surface coatings [5–7], direct surface texturing

* Corresponding authors.

E-mail addresses: matic.moze@fs.uni-lj.si (M. Može), peter.gregorcic@fs.uni-lj.si (P. Gregorčič).

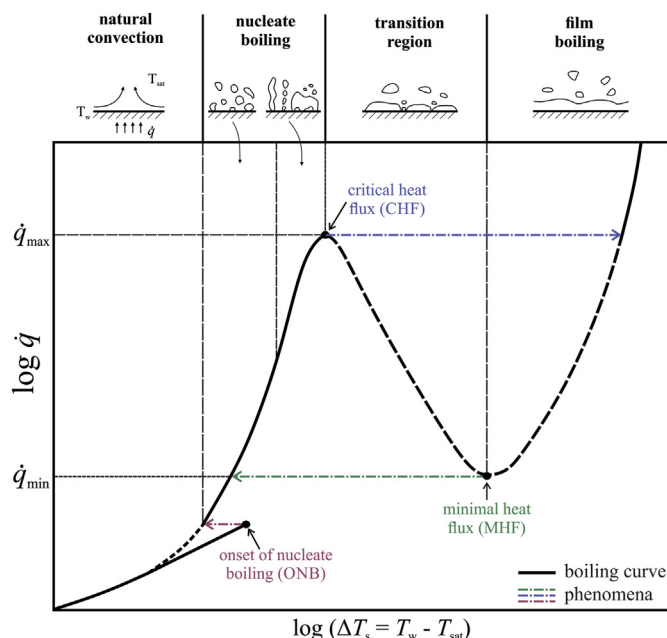


Fig. 1. Typical pool-boiling curve with presentation of different surface-fluid interface scenarios.

[8,9] and fabrication of macro-, micro- and nanoscopic surface structures [10–12].

Over the past decades, many approaches have been developed to improve the following key boiling heat transfer parameters: the heat transfer coefficient, point of nucleate boiling onset and critical heat flux. This has been achieved through fabrication of micro and nanostructures [4,13], wettability modification [6,14], nanoparticle deposition [15,16] and nanowire/nanorod fabrication [12,17]. Besides improving the heat transfer parameters, other aspects of the boiling surface are important from a practical application standpoint. They include surface stability, price and flexibility of the modification process and resistance to fouling and mechanical damage. One of the most commonly used materials in heat transfer applications is copper, which provides extremely high thermal conductivity. Additionally, it is superbly resistant to biofouling and many types of corrosion, resistant to high temperatures and can be easily shaped and joined. While a plethora of surface modification methods exist, especially direct laser texturing is gaining importance due to several advantages over other methods, which include extreme flexibility of patterns and effects that can be produced [18,19] and absence of chemicals in the surface fabrication process (eco-friendliness).

This study has multiple goals. Firstly, pool-boiling heat transfer performance of laser-textured copper surfaces is investigated. Two laser-textured surfaces are fabricated under different processing atmospheres with intentionally created multiscale microcavities. Laser processing parameters were previously optimized and tested on stainless steel [4,8,20]. Here, they are used to induce the multiscale microcavities on the copper surfaces for enhanced nucleate boiling heat transfer. Surface topography and chemical composition are analyzed using scanning-electron microscopy (SEM), energy-dispersive X-ray spectroscopy (EDS), Auger electron spectroscopy (AES) and X-ray

photoelectron spectroscopy (XPS) analysis, 3D optical microscopy and apparent water contact angle (WCA) measurements. Boiling performance of the surfaces is tested using twice-distilled water at atmospheric pressure under saturated conditions. Secondly, boiling tests are repeated multiple times (achieving CHF incipience every time) on the tested surfaces to determine the stability of the boiling curve and hence the surface properties. Finally, the characteristics of the surfaces are compared before and after the boiling process had taken place on them. Changes in surface chemical composition after the boiling experiments are observed and a possible relationship between the changes of the boiling heat transfer, surface chemistry changes and wettability alterations is investigated.

2. Materials and methods

2.1. Sample preparation

Research was carried out on disc-shaped samples with a diameter of 18 mm and thickness of 4 mm made of copper with electrolytic purity (99.9+ % Cu). A type K thermocouple was glued into the hole in each sample. All samples were finely sanded using first P1200 and then P2000 grit sandpaper before subsequent laser treatment. A reference (untreated) sample, denoted as REF, was produced with a surface roughness $S_a = 0.15 \mu\text{m}$.

2.2. Laser texturing

Two samples were laser textured using laser parameters listed in Table 1 and two processing atmospheres (air and argon - an inert atmosphere). The laser processing parameters were optimized within our previous work [4,8]. A nanosecond fiber laser (SPI Lasers, G4, SP-020P-A-HS-S-A-Y) with the wavelength of $\lambda = 1060 \text{ nm}$ was employed for surface processing. The used pulse duration equaled 28 ns at full width at half maximum (FWHM) and 50 ns at 10% peak power, respectively. Average power of the laser pulses equaled 9.2 W with a corresponding beam diameter of $38 \mu\text{m}$. The spot beam diameter $2w_0$ was calculated from focal lens distance of the F-Theta lens ($f_L = 163 \text{ mm}$), beam diameter at the F-Theta lens D and the beam quality factor $M^2 = 1.3$, as $2w_0 = 4M^2\lambda f_L / (\pi D)$. The laser beam was guided across the surface using a scanning head (Raylase, SS-II-E-10) in a way that the distance between two consequent pulses equaled $3 \mu\text{m}$. Both samples were textured in x direction utilizing a variable scanning line separation $\Delta y = \{50 \mu\text{m}, 55 \mu\text{m}, 60 \mu\text{m}\}$ in order to guarantee the appearance multiscale microcavities, as previously explained in detail in Refs. [4, 8]. The average pulse fluence is calculated as $F = Ep / (\pi w_0^2)$, where Ep is used for pulse energy.

2.3. Surface characterization

Surfaces were characterized by using several analytical methods. To reveal the surface morphological modifications, the samples were examined using a SEM (JEOL JSM-6500F) at an accelerating voltage of 15 kV utilizing a secondary electron detector. The roughness parameters (S_a and R_a) were measured by a non-contact Alicona InfiniteFocusSL microscope.

The surface chemistry on an atomic and molecular level were analyzed with different techniques. A dispersive X-ray spectroscopy (EDS;

Table 1

The key processing parameters used for laser-textured surfaces.

Sample	Scanning line separation Δy (μm)	Scanning velocity v (mm s^{-1})	Repetition rate f (kHz)	Pulse fluence F (J cm^{-2})	Processing atmosphere
L1	Variable, 50–55–60	150	50	16.1	Air
L2					Argon

Oxford EDS Inca Energy 450 with Inca X-Sight LN2 detector type) was used, since it presents a very convenient and widely accessible technique. However, it acquires the X-ray signal from one- to several-micrometers thick surface layer [21]. Thus, its signal contains an average of the elemental composition from the modified surface (with a typical thickness of only several hundred nanometers) and unmodified bulk material. One set of EDS measurements was performed at an acceleration voltage of 20 kV, while for the second set this voltage was reduced to 5 kV in order to probe the atomic composition of the region closer to the (modified) surface layer. Since only the uppermost surface layer represents an interface that effects the interaction between the surface and its surroundings (i.e., the working fluid in our case), the atomic composition of the first few nanometers of the surface was additionally examined by an Auger electron spectroscopy (AES; Microlab 310F VG-Scientific SAM) with a depth resolution in the nanometer range. The chemical composition of different copper oxides was analyzed by fitting the narrow-range X-ray photoelectron spectroscopy (XPS) scans of Cu 2p_{3/2} peak. Here, Al-K α radiation at 1486.6 eV with an anode voltage \times emission current 12.5 kV \times 16 mA = 200 W power was used.

The wettability of the surfaces was evaluated at room temperature using twice-distilled water and a goniometer of our own design. Based on the pictures taken with an IDS UI-3060CP camera, analysis and apparent contact angle determination were performed using a MathWorks MATLAB script, similarly as in Ref. [22]. Characteristics of all surfaces were analyzed immediately before the boiling tests and after them to record any changes that would primarily be a consequence of the boiling process.

2.4. Pool-boiling setup

A schematic representation of the pool-boiling experimental setup is shown in Fig. 2. It consists of a cylindrical glass boiling chamber with an inner diameter of 100 mm. During the boiling experiments the chamber was filled halfway with 500 ml of twice-distilled water. Another glass cylinder is mounted around the boiling chamber to minimize heat losses. Heat is supplied to the sample by the means of conduction from the copper heater block with three 400 W AC cartridge heaters. Heat flux is calculated through the spatial temperature profile utilizing the Fourier's law of heat conduction from temperatures, measured in the heater block's stem. The sides of the copper stem are insulated with aerogel fiber mat with a thermal conductivity of

0.016 W m⁻¹ K⁻¹. Since the thermal conductivity of copper is more than a thousand times higher than that of the insulation, one dimensional heat conduction is considered, and lateral heat losses are disregarded as they are negligible. An immersion heater is used to bring the water to the saturation temperature and degas it through vigorous boiling for two hours prior to the start of the measurements. During the measurements, the power of the immersion heater is decreased to a minimum so that the saturated state of the liquid is maintained.

Before every measurement, the surface and the water were cooled down to below 95 °C to ensure that all vapor nuclei in cavities condense. Measurements were performed by continuously increasing the heat flux at the rate of approximately $0.2 \text{ kW m}^{-2} \text{ s}^{-1}$ in the natural convection region and $2 \text{ kW m}^{-2} \text{ s}^{-1}$ in the nucleate boiling region. Preliminary measurements have confirmed that the results obtained using this methodology do not differ from the results obtained in a steady state (see Supplementary Information Fig. S2). On laser-textured surfaces, boiling heat transfer was first evaluated through several experimental runs up to 1500 kW m^{-2} . After that, CHF was measured and the additional boiling curves were recorded in subsequent tests, achieving CHF incipience every time.

As the heating block with the cartridge heaters present a considerable thermal mass, the creation of a vapor film on the surface and transition towards film boiling could not be prevented when the CHF incipience occurred. At this point, the surface was left to cool together with the heating block until the vapor film collapsed. The ongoing phase-change process transitioned towards the film boiling region after the CHF incipience and vapor film formation (approximately along the dashed line between CHF and MHF in Fig. 1). Even though a vapor film formed and persisted on the surface, the surface temperatures did not exceed 320 °C, as the heat supply was turned off immediately after reaching CHF incipience. After the formation of the vapor film, the boiling process continued at a very low heat flux with decreasing temperatures (at an average rate of approximately -0.2 K/s to -0.4 K/s). This process can be roughly described by the green dash-dot line in Fig. 1. Nucleate boiling was reestablished after the disintegration of the vapor film. During the vapor film formation process, the surface temperatures reached 210–320 °C (the higher the CHF value, the higher the surface temperature after the CHF incipience). Typically, the vapor film disintegrated after approximately 10 min.

The relative measurement uncertainty of the heat flux was estimated as 3.6% at 200 kW m⁻² and 2.1% above 1 MW m⁻². The relative

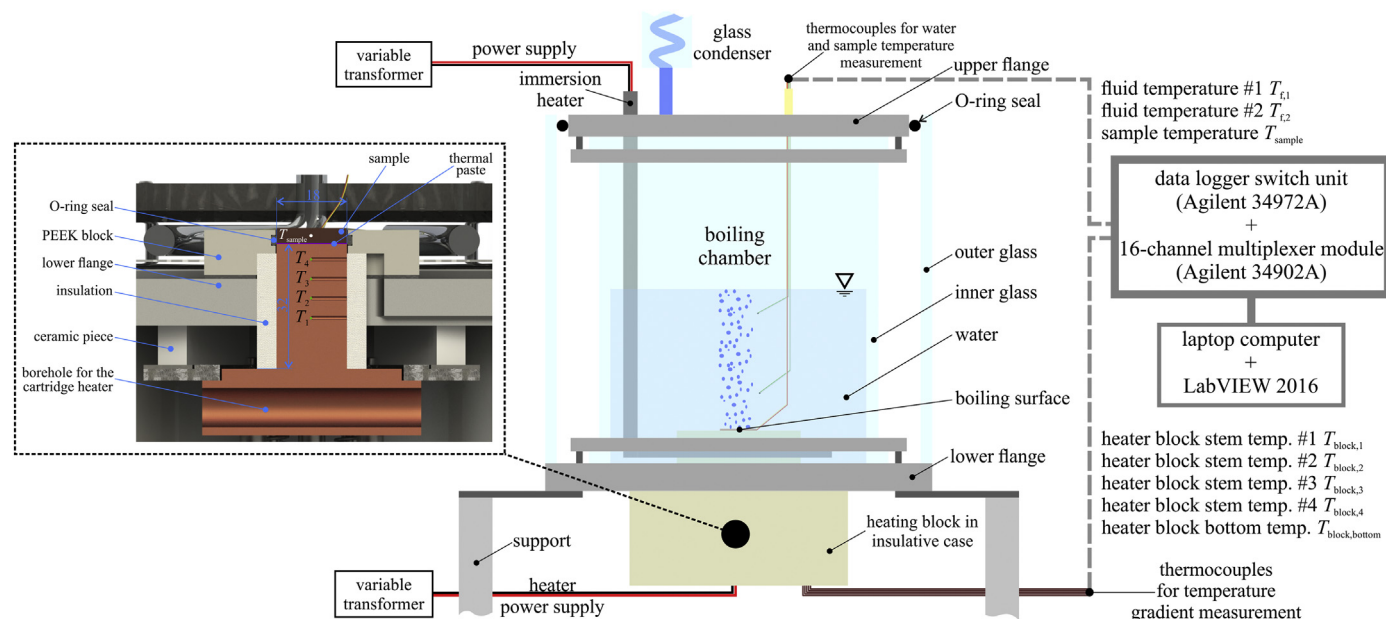


Fig. 2. Pool-boiling experimental setup.

Table 2
List of surfaces used in the experiments.

Sample	Treatment	Microcavity size range (μm)
REF	Mechanical (sanding with P2000 grit)	N/A
L1	Laser texturing (microcavities produced in air)	0.35–5.6
L2	Laser texturing (microcavities produced in argon)	0.37–4.9

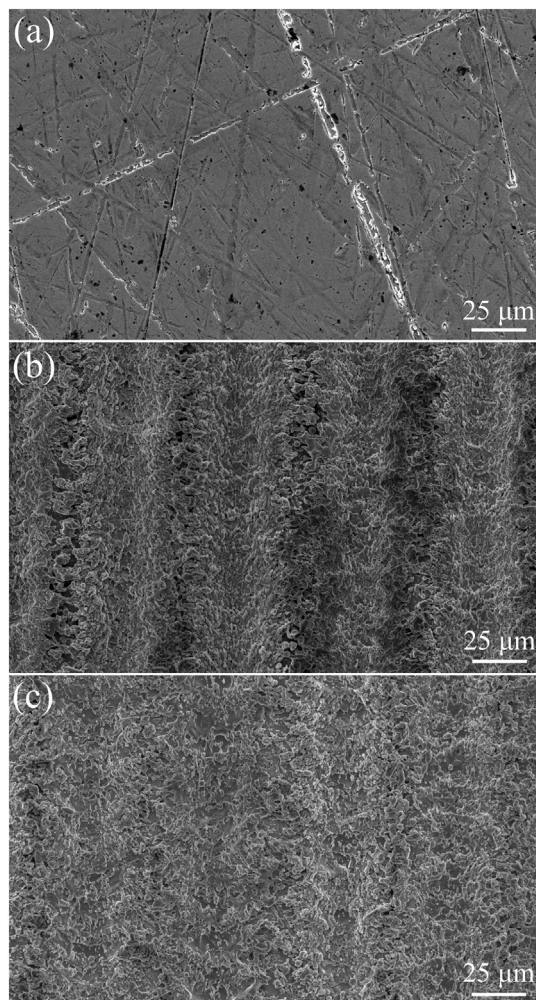


Fig. 3. SEM images of (a) the reference surface REF, (b) laser-textured surface in air L1 and (c) laser-textured surface in argon L2.

measurement uncertainty of the surface superheat was calculated to be 6.2% at 1 MW m^{-2} and the heat transfer coefficient relative measurement uncertainty was 6.5% at 1 MW m^{-2} .

3. Results

3.1. Surface characteristics

The surfaces used in boiling experiments are summarized in Table 2, while the corresponding SEM images are shown in Fig. 3.

The presence of multiscale microcavities discussed in previous sections was confirmed using SEM imaging (see Supplementary Information, Figs. S3 and S4). The size range of microcavity diameters on every surface was measured on multiple SEM images and is listed in Table 2 as minimum and maximum measured values.

Laser-texturing parameters were chosen based on preliminary testing and in accordance with findings of our previous research made on stainless steel [4,8,20]. We have shown that so-called multiscale

microcavities form on the ridge of resolidified material between two parallel laser beam scanning lines on the surface of the sample. The material (metal) is ablated, partially vaporized and molten due to high peak intensities (exceeding 10^9 W cm^{-2}) of laser pulses. Rapid vaporization itself causes recoil pressure, which exceeds the surface tension pressure of the liquefied metal and therefore induces the hydrodynamic motion of liquefied metal towards the side of each laser beam trace [23].

In this study, we have slightly modified the parameters from our previous work so that multiscale microcavities with diameters between 0.35 and $5.6 \mu\text{m}$ (see Fig. S1 in Supplementary Information) formed on the copper samples between parallel laser scanning lines due to overlapping of the resolidified material. A graphic explanation of the microcavity formation process is shown in Fig. 4. However, microcavities only form when a specific combination of laser beam parameters (particularly, pulse fluence [22]) and texturing pattern geometry is used. Therefore, we used variable spacing of the scanning line separation ($50\text{--}55\text{--}60 \mu\text{m}$) to ensure that microcavities would surely form and to achieve a wide range of their radii (e.g., see Ref. [4], including the complementary Supplementary Information).

Previous studies [4,8] have shown that the multiscale microcavities significantly enhance the boiling process as they serve as potential and preferential active nucleation sites from which the bubbles grow. Moreover, some cavities are interconnected between each other, thus forming vapor-trapping pockets inside the boiling surface, while their dimensions depend on the laser-texturing parameters [4]. Thus, these parameters need to be tailored to the material of the sample.

Hsu [24] developed a criterion for the size range of microcavities, which determines whether they can serve as active nucleation sites for a given combination of the working fluid, surface wettability and surface superheat. Based on this theory, the most appropriate diameters of microcavities for them to serve as active nucleation sites in pool boiling of water are in the micrometer range with the exact numbers being dependent on the surface wettability. By producing an abundance of microcavities of various sizes within this micrometer size range, we managed to reduce or possibly eliminate the effect of surface wettability as nucleation can take place from preferential microcavities regardless of the wettability with plenty microcavities available on the surface for any given required diameter.

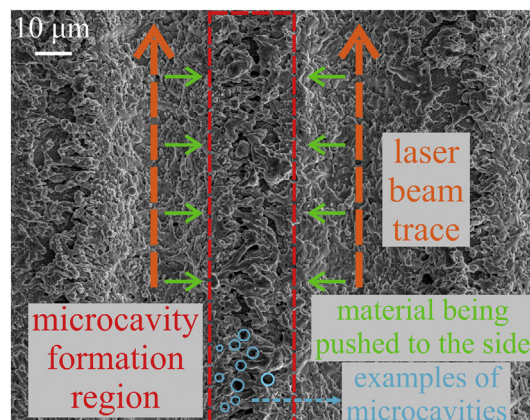


Fig. 4. Multiscale microcavity formation process.

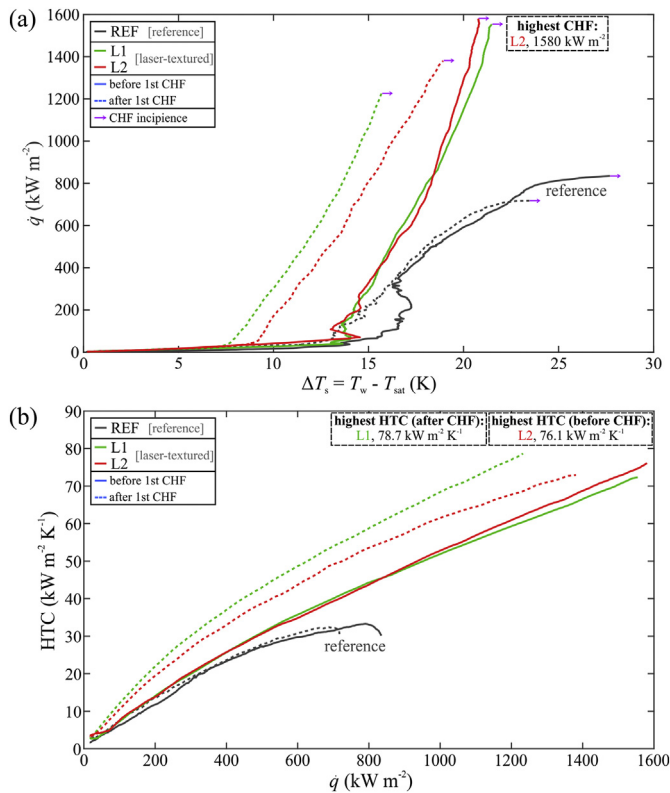


Fig. 5. Boiling heat transfer performance before and after the first incidence of CHF shown as (a) boiling curves and (b) heat transfer coefficients.

3.2. Pool-boiling performance

Boiling performance of each surface was evaluated multiple times. Fig. 5 shows the boiling curves (i.e., heat flux as a function of surface superheat) recorded on all surfaces during the experimental run when the CHF was first reached and during the first subsequent experimental run. A significant shift in boiling curves was recorded and will be discussed in detail later.

Boiling heat transfer parameters recorded at the first CHF incidence and during the first subsequent experimental run are summarized in Table 3. While the highest HTC value for surface L1 and L2 was recorded at the CHF incidence, the highest HTC values on the reference surface were recorded at a heat flux approximately 10% below CHF.

The values in Table 3 show that CHF decreases on all surfaces following its first incidence. However, since the boiling curves are shifted towards lower superheats, the HTC values do not necessarily decrease by a large margin; in the case of surface L1, HTC actually increases. Laser-textured surfaces also show significant heat transfer parameter improvements with CHF and HTC increases in comparison with the reference surface of 86–89% and 117–129%, respectively (both before the first CHF incidence).

Table 3

Boiling heat transfer parameters before and after the first CHF incidence.

Sample	Before first CHF			After first CHF		
	CHF (kW m^{-2})	ΔT_s (K)	max. HTC ($\text{kW m}^{-2} \text{K}^{-1}$)	CHF (kW m^{-2})	ΔT_s (K)	max. HTC ($\text{kW m}^{-2} \text{K}^{-1}$)
REF	835	27.7	33.3 [@ 791 kW m^{-2}]	717	23.5	32.4 [@ 684 kW m^{-2}]
L1	1554	21.5	72.3 [@ CHF]	1232	15.7	78.7 [@ CHF]
L2	1580	20.8	76.1 [@ CHF]	1381	18.9	73.0 [@ CHF]

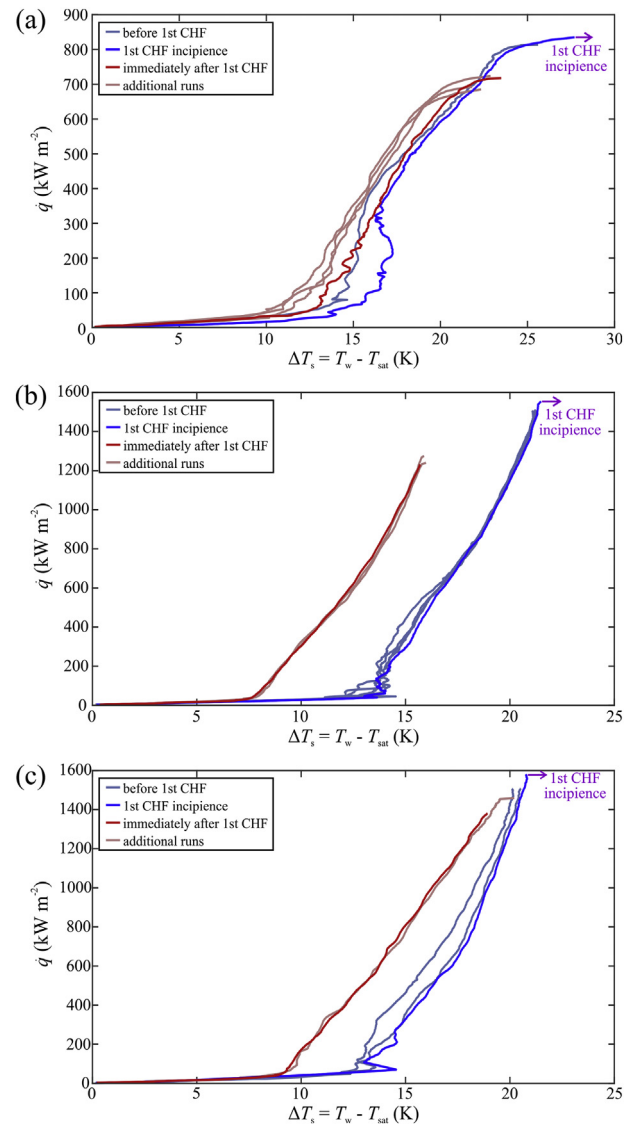


Fig. 6. Boiling curve stability in repeated experimental runs on (a) the reference surface REF, (b) laser-textured surface in air L1 and (c) laser-textured surface in argon L2.

3.3. Boiling curve and boiling process stability

Due to the observations made during initial experiments with boiling performance of structured surfaces (Fig. 5), additional research was carried out to further analyze the stability of the boiling process and boiling curve shift after the first incidence of CHF. Fig. 6 shows the results of repeated experimental runs on all surfaces. The first incidence of CHF is denoted by purple color; the CHF was also reached during every subsequent experimental run. The incidence of CHF and film boiling did not damage nor destroy the surface. However, the surface characterization, discussed in the next sections, revealed that it

significantly influenced surface morphology, chemistry and wettability.

The reference surface exhibits a slight shift of the boiling curves towards lower superheats with CHF decreasing with every experimental run. On the contrary, the boiling curves on the laser-textured surfaces exhibit excellent stability before and after the first CHF incipience. A shift of boiling curves is again observed and the curves stabilize after undergoing the shift.

3.4. Influence of CHF incipience on surface properties

The atomic composition of all surfaces was examined before and after boiling (after reaching CHF multiple times) by using EDS and XPS. Additionally, all AES results are available in Supplementary Information (Fig. S11 and Table S2). They show the lowest O/Cu ratio (0.72) on the REF surface before boiling. After boiling, this ratio increases to 2.1, which is also the highest O/Cu ratio recorded in our analysis. From these results (see Supplementary Information, Table S2), it follows that the O/Cu ratio decreases after boiling for both laser-textured surfaces. This suggests surface deoxidation when CHF is achieved. The content of carbon most probably corresponds to surface contamination that may happen even during their storage (after boiling and before surface analysis) [25]. Our analysis focused primarily on the content of oxygen and copper (see also Supplementary Information, Tables S2–S4).

The surface atomic composition was also analyzed in parallel by using EDS, since this method is often used [26,27] for surface characterization of laser-textured surfaces due to its simplicity and wide accessibility. As expected, the O/Cu ratios (see Supplementary Information, Tables S3 and S4) are significantly lower as those measured by AES. This happens since EDS acquires X-rays from a much thicker surface layer resulting in an increased amount of the detected Cu atoms (e.g., from the bulk of the material). Reducing the acceleration voltage, as suggested in [27], slightly increases the O/Cu ratio, but it is not able to overcome the deficiency of this technique. Therefore, EDS can be mainly used for a preliminary examination of chemical modifications due to laser-surface interaction and it cannot be used for (any) conclusions regarding the chemical composition of the uppermost layers of molecules/atoms, which are vital for the interaction with the working fluid during boiling.

Copper has two stable oxides: cuprous (Cu_2O , denoted also as Cu(I) oxide) and cupric (CuO , denoted also as Cu(II) oxide) oxide; therefore, the atomic O/Cu ratio should be between 0 (pure copper) and 1 (pure cupric oxide). AES analysis, as already explained, in almost all cases gave this ratio above 1. This suggests that oxygen also has to be bound to other molecules – most probably in the form of oxygen-containing functional groups within organic carbon contamination (e.g., C–O and O–C=O) [25,28,29]. However, the atomic O/Cu ratio can reach values up to 2 also in case of Cu(II) hydroxide ($\text{Cu}(\text{OH})_2$). Thus, to completely understand the influence of the boiling process on the chemical modification of laser-textured surfaces, an XPS analysis is unavoidable.

Typical narrow-scan XPS photopeaks for C 1s and Cu $2p_{3/2}$ are shown in Fig. 7. The C 1s peak was fitted using Shirley-type background and three pure Gaussian line shapes (defined by GL(0) in CasaXPS), as suggested in Ref. [29]. A main peak at 284.7 eV was attributed to hydrocarbon chains or the graphitic structure (C–C/C–H) and it was used for charge neutralization. The other two contributions were attributed to the oxygen containing functional groups C–O and O–C=O, and were constrained at around 1.5 eV, and 3.6 eV from the C–C/C–H components, respectively [28,29] (all fitting parameters are summarized in Supplementary Information, Table S5).

The narrow scan of the Cu 2p spectra for the laser-processed surfaces before boiling show two peaks [e.g., see Fig. 7(b)]. The signal with peak between 932 and 934 eV corresponds to Cu $2p_{3/2}$ level and is composed of peaks corresponding to Cu metal, Cu(I) oxide, Cu(II) oxide and Cu(II) hydroxide [30,31]. However, the Cu $2p_{3/2}$ level in Cu(II) oxide and Cu(II) hydroxide results in the presence of a shake-up

satellite at approximately 10 eV higher binding energies than the $2p_{3/2}$ peak [31,32]. The presence of this shake-up satellite peak is, therefore, a clear indicator of the presence of Cu(II) oxide and/or Cu(II) hydroxide.

As clearly visible from Fig. 7(b,c), the shake-up satellite peak disappears after boiling experiments on the L1 sample. Similar behavior is also observed on the L2 sample (see Fig. S18 in the Supplementary Information), although the sum of the CuO and the $\text{Cu}(\text{OH})_2$ content is much lower on the L2 sample even before boiling. This suggests that the boiling process results in deoxidation of Cu(II) oxide and hydroxide into the Cu(I) oxide and/or Cu metal.

As shown by Biesinger et al. [31,33], the relative concentration of the Cu metal and Cu(I) oxide species on the surface, $\kappa_{0,1}$, can be determined by the areas A under the main Cu $2p_{3/2}$ peak and B under the shake-up satellite peak [Fig. 7(a)] as:

$$\kappa_{0,1} = \frac{A - \eta B}{A + B} \quad (1)$$

where factor η was experimentally determined to be in the range between 1.57 ± 0.1 for pure Cu(II) hydroxide and 1.89 ± 0.08 for pure Cu(II) oxide [31]. The relative concentration of the Cu(II) species equals $\kappa_{II} = 1 - \kappa_{0,1}$. By using Eq. (1), we calculated the atomic percentage of Cu metal and Cu(I) oxide species as well as Cu(II) oxide and hydroxide species of all the tested surfaces before and after boiling. The range of Cu/Cu₂O atomic concentration calculated by Eq. (1) from XPS spectra of all the used surfaces is shown in the third column of the Table S6 in the Supplementary Information.

However, the relative concentration of the Cu(II) oxide and hydroxide on the surface can be determined only by appropriate fitting of the main and the shake-up satellite peaks within the Cu $2p_{3/2}$ spectra. This was also done by using a Shirley-type background. We followed the fitting parameters suggested in the Ref. [31]. For determination of Cu metal and Cu(I) oxide species, two Gaussian (10%) – Lorentzian (90%) peak shapes (defined by GL(90) in CasaXPS) were constructed. The Cu metal peak was constrained within 932.60–932.65 eV, while the Cu(I) oxide peak was constrained within 932.0–932.65 eV. However, the statistically similar binding-energy values of Cu metal and Cu(I) oxide makes it impossible to distinguish between these two species from fitting the Cu $2p_{3/2}$ peak [31]. Thus, we have summed the concentrations obtained by both peaks.

For the deconvolution of Cu(II) oxide, four Gaussian (70%) – Lorentzian (30%) peak shapes (defined as GL(30) in CasaXPS) were constructed. They were constrained at around 1.13 eV, 7.89 eV, 9.02, and 11.07 from the Cu metal component, respectively. The sum of these peaks fitting the main and the shake-up satellite peaks gives the concentration of the cupric oxide. The Cu(II) hydroxide was determined by using another four peaks (defined by GL(30) peak shape in CasaXPS) that were constrained at around 2.04 eV, 6.67 eV, 9.57 eV, and 11.49 eV from the Cu metal peak, respectively. These peaks together were used to determine the concentration of the Cu(II) hydroxide on each of the tested samples. The peaks used for the deconvolution of the $2p_{3/2}$ spectra are shown in Fig. 7(b,c).

The results, summarized in Fig. 8 (and in Supplementary Information, Table S6) reveal that different laser-processing parameters result in different amounts of copper oxides and hydroxides. The Table S6 (Supplementary Information) clearly shows that the values, obtained by the deconvolution of the XPS signal, match the values, calculated by using Eq. (1), well.

Different starting amount of CuO on the laser-textured surfaces correlates well with the available literature [34,35]. Predominantly CuO and $\text{Cu}(\text{OH})_2$ form on the surface, which was textured under air atmosphere, whereas a large amount of Cu_2O is present on the sample, fabricated under the inert argon atmosphere with a negligible oxygen content.

Results clearly indicate that a significant part of the cupric oxide is converted into the cuprous oxide during boiling on all samples.

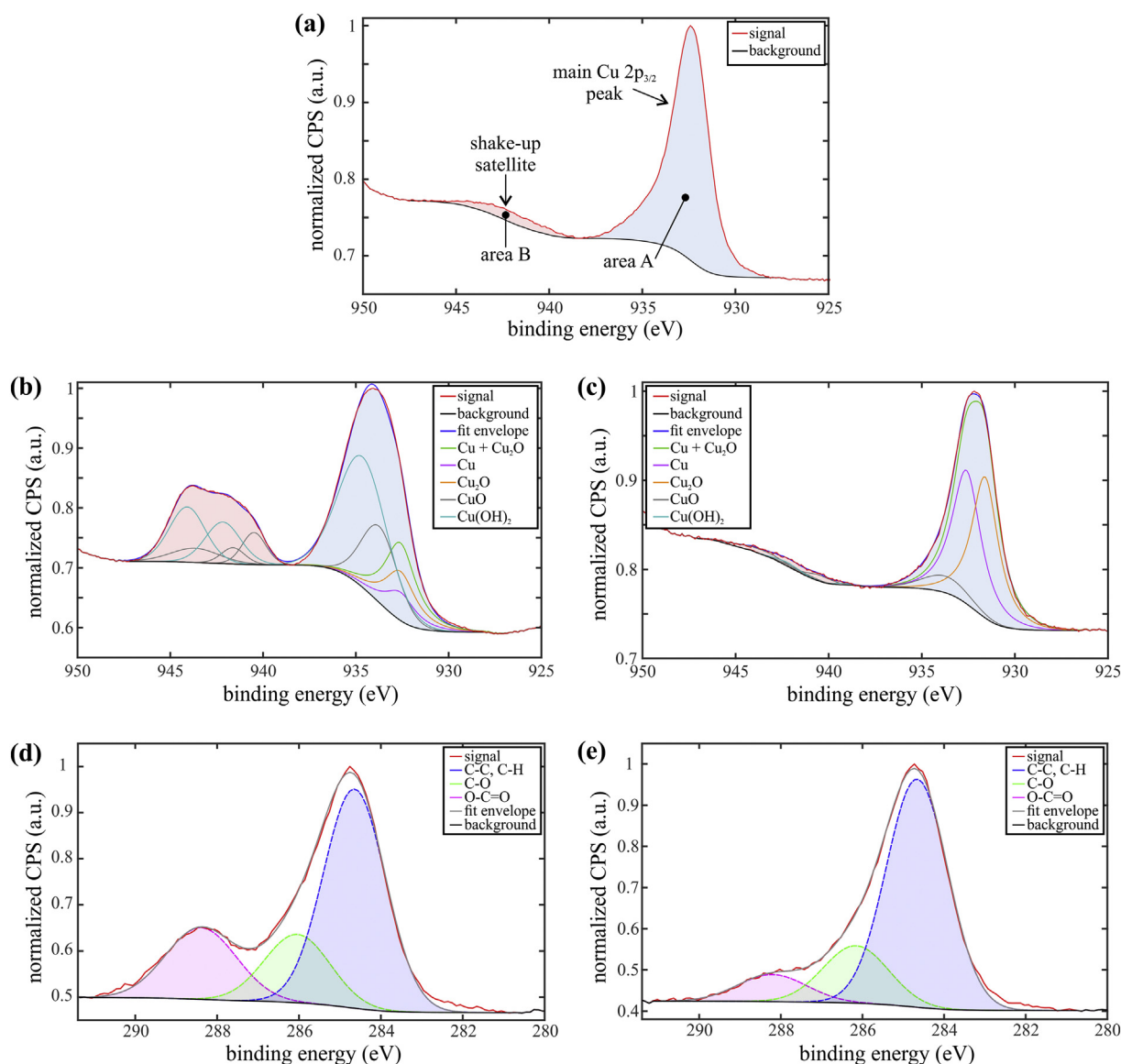


Fig. 7. Results of the XPS analysis of the surface composition. (a) Cu 2p_{3/2} main peak and its shake-up satellite on the surface REF before boiling; Cu 2p_{3/2} main peak and its shake-up satellite (with corresponding deconvolution) on the surface L1 (b) before and (c) after boiling; deconvolution of the C 1s peak on surface L1 (d) before and (e) after boiling.

Moreover, the content of Cu(OH)₂ decreases post-boiling on all surfaces, which corresponds to reduction of Cu(OH)₂ into Cu(I) oxide and Cu metal. This is additionally confirmed by high magnification SEM images, shown in Fig. 9 (see also Figs. S5-S10 in the Supplementary Information), where the typical shape of both oxides is clearly distinguishable. In our case, Cu(II) oxide and hydroxide primarily form thin needle-like structures (as in Refs. [36–38]), whereas Cu(I) oxide manifests itself as sub-micron sized cubes or (truncated) octahedra (as in Refs. [39–41]).

The apparent contact angle of water (WCA) was measured on every surface prior to the boiling experiments and immediately after them. Ten drops were deposited onto various parts of the surface and the contact angles were recorded and averaged; they are depicted in Fig. 10. The wettability of all tested surfaces decreases after boiling. Laser-textured surfaces are hydrophilic after processing and before boiling. These surfaces are covered with high-surface-energy oxides which form during laser texturing [21,26] when the surface material is molten and ablated. After being exposed to high temperatures during repeated CHF incipience, saturated twice-distilled water and the boiling process for several hours, the wettability of surfaces changes from a

hydrophilic towards a hydrophobic state with contacts angles between 84° and 121° (Fig. 10).

4. Discussion

The results of pool-boiling experiments on laser-textured surfaces show that laser processing can be utilized to fabricate metal surfaces for significantly enhanced nucleate boiling heat transfer. The latter is achieved mainly by providing preferential active nucleation sites in the form of microcavities or similar (micro)structures. In this way, the laser texturing gave us control over the locations where bubbles would form and grow on the surface. Multiscale microcavities have been previously proposed and fabricated on stainless steel [4,8] to enhance the boiling performance and control. Current results prove that the same methods can also be applied to copper through minor modifications of the laser-texturing parameters due to different material and optical properties of copper as opposed to stainless steel. The results of boiling experiments indicate that the laser-processing atmosphere had only a minor influence on the boiling heat transfer performance, since the boiling heat transfer is significantly enhanced as long as appropriately sized

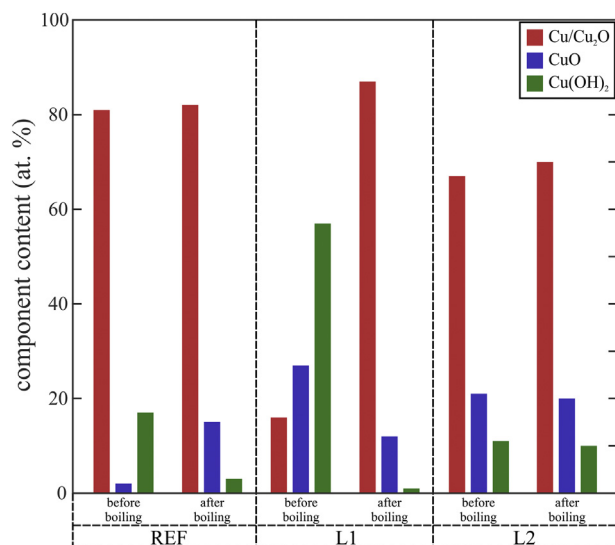


Fig. 8. Comparison of the Cu/Cu₂O, CuO and Cu(OH)₂ content before and after boiling.

microcavities are present on the surface. This is proved by experiments on surfaces L1 and L2, which provide a similar enhancement over the untreated reference surface.

Possible reasons for the shift in boiling curves were researched systematically. Leakage of substances from materials used in the construction of the experimental setup into the water could cause a change in its properties. This was, however, disproven by additional experiments where the water was changed after two experimental runs. If there were any impurities in the water significantly impacting boiling heat transfer, the boiling curves would shift back to their original position after the water was replaced. However, the boiling curves of experiments with replaced water closely matched that of the experimental run with the original water after the first CHF incipience.

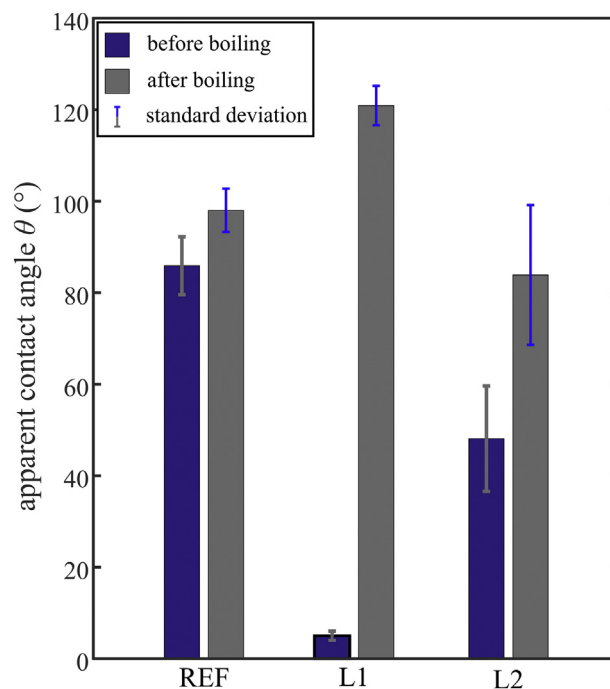


Fig. 10. Apparent water contact angle on all surfaces immediately before and immediately after boiling experiments.

Detailed results of this additional experiment are available in the Supplementary Information (Fig. S19).

In addition to nucleate boiling being a very intensive process, high temperatures are reached during the CHF phenomenon when the process transitions towards film boiling (in the region of 210–320 °C). This is likely results in low-temperature annealing of the surface, which causes a partial conversion of copper oxides from one form to another in addition to the reduction of the Cu(OH)₂. As mentioned previously,

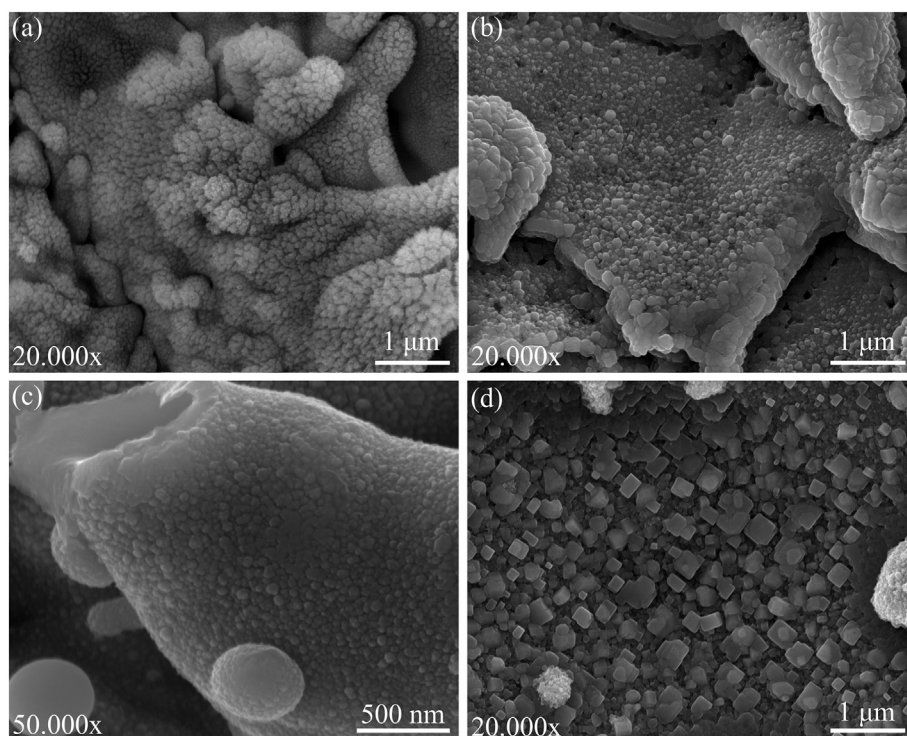


Fig. 9. Morphology of laser-textured surfaces L1 (a) before and (b) after boiling and L2 (c) before and (d) after boiling.

these high temperatures persisted on the surface after CHF incipience for a significant amount of time. Hyam et al. [38] have shown that heat treatment of $\text{Cu}(\text{OH})_2$ in different atmospheres causes a transformation into CuO or reduction to Cu_2O . Tobin et al. [42] have shown that CuO partially converts to Cu_2O alongside with the appearance surface deoxidation during vacuum annealing of copper at 200 °C. Li et al. [43], Honkanen et al. [44], Figueiredo et al. [45] and Figueira et al. [46] have shown that Cu_2O forms during low-temperature annealing of Cu samples in air atmosphere (from below 200 °C to roughly 300 °C) and that CuO preferentially forms at higher temperatures (above 350 °C). This appears to confirm the transformation of $\text{Cu}(\text{II})$ oxide and hydroxide (formed during laser texturing due to very high temperatures) into $\text{Cu}(\text{I})$ oxide and, presumably, Cu metal during the film boiling after the incipience of CHF. It also appears that this transformation is complete within one incipience of CHF and subsequent film boiling on samples L1 and L2 as higher temperatures are reached during film boiling (up to 320 °C) due to higher CHF. On the untreated reference surface, CHF values decrease every time the transition into film boiling is reached, which is likely due to slightly lower temperatures of the surface during film boiling (210–250 °C) and, therefore, incomplete annealing.

The decrease in wettability of laser-textured surfaces can be partially explained by a reduction of both oxygen and CuO content as recorded by the AES and XPS analyses. This also correlates well with the shift of the boiling curves towards lower superheats and lower CHF values. Extensive research [5,6,14] has shown that hydrophobic surfaces exhibit lower superheats and thus provide higher heat transfer coefficients compared to hydrophilic surfaces with similar topographical features. However, hydrophobic surfaces also exhibit reduced CHF values compared to hydrophilic surfaces, which was also observed in our case. The exact classification of Cu_2O , CuO and $\text{Cu}(\text{OH})_2$ as hydrophilic or hydrophobic materials is rather impossible. By default, both oxides should exhibit (super)hydrophilicity due to their high surface energy. However, conflicting literature exists where Cu_2O has been classified as hydrophobic [34,47], while Chang et al. [48] reports that even CuO exhibits hydrophobicity after low-temperature annealing at 100 °C without the formation of Cu_2O (albeit in air atmosphere). $\text{Cu}(\text{OH})_2$ is quite consistently characterized as (super)hydrophilic when it takes the form of (nano)needles [49,50]. Generally, wettability transition from hydrophilic towards hydrophobic after CHF incipience goes hand-in-hand with the decrease of $\text{Cu}(\text{OH})_2$ and CuO in our study. We can conclude that the wettability of the surface is not only dependent upon the chemical composition of the surface, but also on its micro- and nanostructure and roughness [51,52]. As the morphology of copper compounds covering the surface changes after the CHF incipience (alongside the transformation between the three forms), this contributes to the wettability change as well.

The change in boiling heat transfer behavior of surfaces in long-term tests, repeated experiments or due to simulated aging has been noticed by other researchers [2,3,53–55], but was not necessarily discussed and/or analyzed further. In his PhD thesis, Zuber [56] mentions the effect of surface aging on boiling heat transfer parameters, specifically that after prolonged boiling on a surface, the effect of roughness on the number of active nucleation sites [54] and the surface superheat at a given heat flux [53] disappears. These parameters are supposedly independent of the initial surface roughness and are only influenced by the material of the boiling surface. Oxide formation during prolonged boiling process causes additional thermal resistance, which appears to be a function of the thermal conductivity of the oxide alone. After the boiling process has taken place on the surface for a long time, the number of active nucleation sites approaches a limiting value and the boiling curve stabilizes with decreasing heat transfer coefficients. Despite these interesting findings and their obvious importance for practical applications of engineered surfaces for enhanced heat transfer, no attempts have been made until now to explain the behavior of surfaces during prolonged boiling experiments using surface chemistry analysis and for various surface treatments.

5. Conclusions

Laser texturing was used to fabricate copper surfaces for enhanced boiling heat transfer. Previously developed method of microcavity fabrication was applied to copper for the first time. Nucleate boiling heat transfer performance of surfaces was evaluated at atmospheric pressure and saturated conditions using twice-distilled water as the working fluid. Enhanced boiling heat transfer resulting in increased CHF and HTC values was recorded on laser-textured surfaces due to the presence of microcavities, which served as preferential nucleation sites. We show a trend of changes in boiling performance of copper surfaces in repeated boiling experiments with a special emphasis on the effect of CHF incipience on both pool-boiling heat transfer and on surface chemistry and wettability after the first incipience of CHF. A shift in the boiling curve was noticed after the first CHF incipience and researched through further experiments with repeated experimental runs. The results of our work lead to the following conclusions:

- Laser texturing improves boiling heat transfer during nucleate boiling. Both laser-textured surfaces exhibited a CHF enhancement of nearly 90% and an HTC increase of over 115% in comparison with the bare reference surface. Intentionally produced microcavities and thus greatly increased number of active nucleation sites are the key reason for enhanced boiling heat transfer.
- Boiling surfaces underwent surface chemistry and morphology changes after the first incipience of CHF as a consequence of high temperatures due to the presence of an insulative vapor film. This caused the surface composition to change with a conversion of $\text{Cu}(\text{II})$ oxide and hydroxide species into $\text{Cu}(\text{I})$ oxide and Cu metal species detected especially on laser-textured surfaces. This was confirmed both through XPS analysis and observations using high magnification SEM images.
- Results from the literature confirm that the temperatures in the range of 210–320 °C reached during the transition into film boiling and the lifetime of the vapor film until its disintegration (approx. 10 min) are appropriate for the oxide and hydroxide transformations to take place. The influence of the atmosphere is debatable, since a water vapor atmosphere was present as opposed to vacuum or air.
- Due to surface chemistry and morphology changes, the wettability of surfaces changed with surfaces transitioning from hydrophilicity (before boiling) towards hydrophobicity (after boiling).
- Altogether, these changes in surface's interaction with the surrounding fluid resulted in changes in boiling heat transfer performance with the CHF decreasing during measurements performed after its first incipience. The boiling curve shifted towards lower superheats, which resulted in the maximal HTC remaining nearly unchanged.
- The results of boiling curve stability analysis through repeated experimental runs show that a shift in boiling curves occurs on every surface. However, the reference surface displayed a tendency of constant shifts with every experimental run, whereas the shift occurs just once on the laser-textured surfaces (the boiling curve becomes largely stable thereafter). This is attributed to higher surface temperatures during the transition into film boiling on laser-textured surfaces and hence a faster and more complete transformation of oxides from CuO into Cu_2O and the accompanying reduction of $\text{Cu}(\text{OH})_2$ to Cu_2O . Additionally, the amount of $\text{Cu}(\text{II})$ oxide and hydroxide is low on the reference surface both before and after boiling.

Acknowledgments

The authors acknowledge the financial support from the state budget by the Slovenian Research Agency (Program/Project Nos. P2-0223, P2-0392, P2-0132 and Z2-9215). The authors would also like to thank SPI Lasers Ltd. for their support of the research project *Surface functionalization by nanosecond fiber laser texturing (nsFLaT)*.

Appendix A. Supplementary data

Supplementary data to this article can be found online at <https://doi.org/10.1016/j.apsusc.2019.06.068>.

References

- [1] S. Nukiyama, The maximum and minimum values of the heat Q transmitted from metal to boiling water under atmospheric pressure, *Int. J. Heat Mass Transf.* 9 (1966) 1419–1433, [https://doi.org/10.1016/0017-9310\(66\)90138-4](https://doi.org/10.1016/0017-9310(66)90138-4).
- [2] A.M. Rishi, A. Gupta, S.G. Kandlikar, Improving aging performance of electro-deposited copper coatings during pool boiling, *Appl. Therm. Eng.* 140 (2018) 406–414, <https://doi.org/10.1016/j.applthermaleng.2018.05.061>.
- [3] C.Y. Lee, B.J. Zhang, K.J. Kim, Morphological change of plain and nano-porous surfaces during boiling and its effect on nucleate pool boiling heat transfer, *Exp. Thermal Fluid Sci.* 40 (2012) 150–158, <https://doi.org/10.1016/j.expthermflsci.2012.02.011>.
- [4] P. Gregorčič, M. Zupančič, I. Golobič, Scalable surface microstructuring by a fiber laser for controlled nucleate boiling performance of high- and low-surface-tension fluids, *Sci. Rep.* 8 (2018), <https://doi.org/10.1038/s41598-018-25843-5>.
- [5] H.T. Phan, N. Caney, P. Marty, S. Colasson, J. Gavillet, Surface wettability control by nanocoating: the effects on pool boiling heat transfer and nucleation mechanism, *Int. J. Heat Mass Transf.* 52 (2009) 5459–5471, <https://doi.org/10.1016/j.ijheatmasstransfer.2009.06.032>.
- [6] A.R. Betz, J. Jenkins, C.J. Kim, D. Attinger, Boiling heat transfer on super-hydrophilic, superhydrophobic, and superbiphilic surfaces, *Int. J. Heat Mass Transf.* 57 (2013) 733–741, <https://doi.org/10.1016/j.ijheatmasstransfer.2012.10.080>.
- [7] A.R. Betz, J. Xu, H. Qiu, D. Attinger, Do surfaces with mixed hydrophilic and hydrophobic areas enhance pool boiling? *Appl. Phys. Lett.* 97 (2010) 13–16, <https://doi.org/10.1063/1.3485057>.
- [8] M. Zupančič, M. Može, P. Gregorčič, I. Golobič, Nanosecond laser texturing of uniformly and non-uniformly wettable micro structured metal surfaces for enhanced boiling heat transfer, *Appl. Surf. Sci.* 399 (2017) 480–490, <https://doi.org/10.1016/j.apsusc.2016.12.120>.
- [9] C.M. Kruse, T. Anderson, C. Wilson, C. Zuhlke, D. Alexander, G. Gogos, S. Ndao, Enhanced pool-boiling heat transfer and critical heat flux on femtosecond laser processed stainless steel surfaces, *Int. J. Heat Mass Transf.* 82 (2015) 109–116, <https://doi.org/10.1016/j.ijheatmasstransfer.2014.11.023>.
- [10] M. Shojaeian, A. Koşar, Pool boiling and flow boiling on micro- and nanostructured surfaces, *Exp. Thermal Fluid Sci.* 63 (2015) 45–73, <https://doi.org/10.1016/j.expthermflsci.2014.12.016>.
- [11] H. Honda, H. Takamastu, J.J. Wei, Enhanced boiling of FC-72 on silicon chips with micro-pin-fins and submicron-scale roughness, *J. Heat Transf.* 124 (2002) 383, <https://doi.org/10.1115/1.1447937>.
- [12] D. Il Shim, G. Choi, N. Lee, T. Kim, B.S. Kim, H.H. Cho, Enhancement of pool boiling heat transfer using aligned silicon nanowire arrays, *ACS Appl. Mater. Interfaces* 9 (2017) 17595–17602, <https://doi.org/10.1021/acsaami.7b01929>.
- [13] Y. Zhang, J. Zhou, W. Zhou, B. Qi, J. Wei, CHF correlation of boiling in FC-72 with micro-pin-fins for electronics cooling, *Appl. Therm. Eng.* 138 (2018) 494–500, <https://doi.org/10.1016/j.applthermaleng.2018.04.053>.
- [14] M. Zupančič, M. Steinbücher, P. Gregorčič, I. Golobič, Enhanced pool-boiling heat transfer on laser-made hydrophobic/superhydrophilic polydimethylsiloxane-silica patterned surfaces, *Appl. Therm. Eng.* 91 (2015) 288–297, <https://doi.org/10.1016/j.applthermaleng.2015.08.026>.
- [15] Z. Cao, C. Preger, Z. Wu, S. Abbood, M.E. Messing, K. Deppert, B. Sundén, Pool boiling heat transfer of water on copper surfaces with nanoparticles coating, *ASME Int. Mech. Eng. Congr. Expo. Proc.* 8 (2017) 1–8, <https://doi.org/10.1115/IMECE2017-71303>.
- [16] S.J. Kim, I.C. Bang, J. Buongiorno, L.W. Hu, Effects of nanoparticle deposition on surface wettability influencing boiling heat transfer in nanofluids, *Appl. Phys. Lett.* 89 (2006), <https://doi.org/10.1063/1.2360892>.
- [17] B. Shi, Y.-B. Wang, K. Chen, Pool boiling heat transfer enhancement with copper nanowire arrays, *Appl. Therm. Eng.* 75 (2015) 115–121, <https://doi.org/10.1016/j.applthermaleng.2014.09.040>.
- [18] A.Y. Vorobyev, C. Guo, Multifunctional surfaces produced by femtosecond laser pulses, *J. Appl. Phys.* 117 (2015) 033103, <https://doi.org/10.1063/1.4905616>.
- [19] P. Gregorčič, M. Sedlaček, B. Podgornik, J. Reif, Formation of laser-induced periodic surface structures (LIPSS) on tool steel by multiple picosecond laser pulses of different polarizations, *Appl. Surf. Sci.* 387 (2016) 698–706, <https://doi.org/10.1016/j.apsusc.2016.06.174>.
- [20] M. Zupančič, M. Može, P. Gregorčič, A. Sitar, I. Golobič, Evaluation of enhanced nucleate boiling performance through wall-temperature distributions on PDMS-silica coated and non-coated laser textured stainless steel surfaces, *Int. J. Heat Mass Transf.* 111 (2017) 419–428, <https://doi.org/10.1016/j.ijheatmasstransfer.2017.03.128>.
- [21] S.V. Kirner, T. Wirth, H. Sturm, J. Krüger, J. Bonse, Nanometer-resolved chemical analyses of femtosecond laser-induced periodic surface structures on titanium, *J. Appl. Phys.* 122 (2017) 104901, <https://doi.org/10.1063/1.4993128>.
- [22] P. Gregorčič, M. Conradi, L. Hribar, M. Hočevar, Long-term influence of laser-processing parameters on (super)hydrophobicity development and stability of stainless-steel surfaces, *Materials (Basel)* 11 (2018), <https://doi.org/10.3390/ma11112240>.
- [23] J. Long, Z. Cao, C. Lin, C. Zhou, Z. He, X. Xie, Formation mechanism of hierarchical micro- and nanostructures on copper induced by low-cost nanosecond lasers, *Appl. Surf. Sci.* 464 (2019) 412–421, <https://doi.org/10.1016/j.apsusc.2018.09.055>.
- [24] Y.Y. Hsu, On the size range of active nucleation cavities on a heating surface, *J. Heat Transf.* 84 (1962) 207–213.
- [25] J. Long, M. Zhong, P. Fan, D. Gong, H. Zhang, Wettability conversion of ultrafast laser structured copper surface, *J. Laser Appl.* 27 (2015) S29107, <https://doi.org/10.2351/1.4906477>.
- [26] P. Gregorčič, B. Šetina-Batič, M. Hočevar, Controlling the stainless steel surface wettability by nanosecond direct laser texturing at high fluences, *Appl. Phys. A Mater. Sci. Process.* 123 (2017) 0, <https://doi.org/10.1007/s00339-017-1392-5>.
- [27] J. Bonse, S.V. Kirner, M. Griepentrog, D. Spaltmann, J. Krüger, Femtosecond laser texturing of surfaces for tribological applications, *Materials (Basel)* 11 (2018) 1–19, <https://doi.org/10.3390/ma11050801>.
- [28] E. McCafferty, J.P. Wightman, Determination of the concentration of surface hydroxyl groups on metal oxide films by a quantitative XPS method, *Surf. Interface Anal.* 26 (1998) 549–564, [https://doi.org/10.1002/\(SICI\)1096-9918\(199807\)26:8<549::AID-SIA396>3.3.CO;2-H](https://doi.org/10.1002/(SICI)1096-9918(199807)26:8<549::AID-SIA396>3.3.CO;2-H).
- [29] M. Mantel, J.P. Wightman, Influence of the surface chemistry on the wettability of stainless steel, *Surf. Interface Anal.* 21 (1994) 595–605, <https://doi.org/10.1002/sia.740210902>.
- [30] M.F. Al-Kuhaili, Characterization of copper oxide thin films deposited by the thermal evaporation of cuprous oxide (Cu₂O), *Vacuum* 82 (2008) 623–629, <https://doi.org/10.1016/j.vacuum.2007.10.004>.
- [31] M.C. Biesinger, L.W.M. Lau, A.R. Gerson, R.S.C. Smart, Resolving surface chemical states in XPS analysis of first row transition metals, oxides and hydroxides: Sc, Ti, V, Cu and Zn, *Appl. Surf. Sci.* 257 (2010) 887–898, <https://doi.org/10.1016/j.apsusc.2010.07.086>.
- [32] S. Poulston, P.M. Parlett, P. Stone, M. Bowker, Surface oxidation and reduction of CuO and Cu₂O studied using XPS and XAES, *Surf. Interface Anal.* 24 (1996) 811–820, [https://doi.org/10.1002/\(SICI\)1096-9918\(199611\)24:12<811::AID-SIA191>3.0.CO;2-Z](https://doi.org/10.1002/(SICI)1096-9918(199611)24:12<811::AID-SIA191>3.0.CO;2-Z).
- [33] M.C. Biesinger, B.R. Hart, R. Polack, B.A. Kobe, R.S.C. Smart, Analysis of mineral surface chemistry in flotation separation using imaging XPS, *Miner. Eng.* 20 (2007) 152–162, <https://doi.org/10.1016/j.mineng.2006.08.006>.
- [34] S.L. Shinde, K.K. Nanda, Facile synthesis of large area porous Cu₂O as super hydrophobic yellow-red phosphors, *RSC Adv.* 2 (2012) 3647–3650, <https://doi.org/10.1039/c2ra20066j>.
- [35] G. Panzer, B. Egert, H.P. Schmidt, The stability of CuO and Cu₂O surfaces during argon sputtering studied by XPS and AES, *Surf. Sci.* 151 (1985) 400–408, [https://doi.org/10.1016/0039-6028\(85\)90383-8](https://doi.org/10.1016/0039-6028(85)90383-8).
- [36] D.P. Singh, N. Ali, Synthesis of TiO₂ and CuO nanotubes and nanowires, *Sci. Adv. Mater.* 2 (2010) 295–335, <https://doi.org/10.1166/sam.2010.1095>.
- [37] X. Wang, J. Yang, L. Shi, M. Gao, Surfactant-free synthesis of CuO with controllable morphologies and enhanced photocatalytic property, *Nanoscale Res. Lett.* 11 (2016), <https://doi.org/10.1186/s11671-016-1278-z>.
- [38] R.S. Hyam, J. Lee, E. Cho, J. Khim, H. Lee, Synthesis of copper hydroxide and oxide nanostructures via anodization technique for efficient photocatalytic application, *J. Nanosci. Nanotechnol.* 12 (2012) 8396–8400, <https://doi.org/10.1166/jnn.2012.6673>.
- [39] K.-S. Choi, Shape control of inorganic materials via electrodeposition, *Dalt. Trans.* 0 (2008) 5432, <https://doi.org/10.1039/b807848c>.
- [40] X. Jiang, M. Zhang, S. Shi, G. He, X. Song, Z. Sun, Microstructure and optical properties of nanocrystalline Cu₂O thin films prepared by electrodeposition, *Nanoscale Res. Lett.* 9 (2014) 1–5, <https://doi.org/10.1186/1556-276X-9-219>.
- [41] X. Wang, M. Chen, Y. He, J. Zhu, Shape-controlled preparation of Cu₂O crystals and their growth mechanism, *J. Alloys Compd.* 628 (2015) 50–56, <https://doi.org/10.1016/j.jallcom.2014.11.224>.
- [42] J.P. Tobin, W. Hirschwald, J. Cunningham, XPS and XAES studies of transient enhancement of Cu₁at CuO surfaces during vacuum outgassing, *Appl. Surf. Sci.* 16 (1983) 441–452, [https://doi.org/10.1016/0378-5963\(83\)90085-5](https://doi.org/10.1016/0378-5963(83)90085-5).
- [43] J. Li, J.W. Mayer, E.G. Colgan, Oxidation and protection in copper and copper alloy thin films, *J. Appl. Phys.* 70 (1991) 2820–2827, <https://doi.org/10.1063/1.349344>.
- [44] M. Honkanen, M. Vippola, T. Lepistö, Low temperature oxidation of copper alloys-AEM and AFM characterization, *J. Mater. Sci.* 42 (2007) 4684–4691, <https://doi.org/10.1007/s10853-006-0351-x>.
- [45] V. Figueiredo, E. Elangovan, G. Gonçalves, P. Barquinha, L. Pereira, N. Franco, E. Alves, R. Martins, E. Fortunato, Effect of post-annealing on the properties of copper oxide thin films obtained from the oxidation of evaporated metallic copper, *Appl. Surf. Sci.* 254 (2008) 3949–3954, <https://doi.org/10.1016/j.apsusc.2007.12.019>.
- [46] J. Figueira, J. Loureiro, J. Marques, C. Bianchi, P. Duarte, M. Ruoho, I. Tittonen, I. Ferreira, Optimization of cuprous oxides thin films to be used as thermoelectric touch detectors, *ACS Appl. Mater. Interfaces* 9 (2017) 6520–6529, <https://doi.org/10.1021/acsaami.6b12753>.
- [47] Y. Ding, Y. Li, L. Yang, Z. Li, W. Xin, X. Liu, L. Pan, J. Zhao, The fabrication of controlled coral-like Cu₂O films and their hydrophobic property, *Appl. Surf. Sci.* 266 (2013) 395–399, <https://doi.org/10.1016/j.apsusc.2012.12.043>.
- [48] F.M. Chang, S.L. Cheng, S.J. Hong, Y.J. Sheng, H.K. Tsao, Superhydrophilicity to superhydrophobicity transition of CuO nanowire films, *Appl. Phys. Lett.* 96 (2010), <https://doi.org/10.1063/1.3360847>.
- [49] K.V. Gurav, U.M. Patil, S.W. Shin, G.L. Agawane, M.P. Suryawanshi, S.M. Pawar, P.S. Patil, C.D. Lokhande, J.H. Kim, Room temperature chemical synthesis of Cu (OH)₂ thin films for supercapacitor application, *J. Alloys Compd.* 573 (2013) 27–31, <https://doi.org/10.1016/j.jallcom.2013.03.193>.
- [50] W. Liang, L. Zhu, W. Li, H. Liu, Facile fabrication of a flower-like CuO/Cu(OH)₂ nanorod film with tunable wetting transition and excellent stability, *RSC Adv.* 5

- (2015) 38100–38110, <https://doi.org/10.1039/c5ra04359j>.
- [51] A. Marmur, Solid-surface characterization by wetting, *Annu. Rev. Mater. Res.* 39 (2009) 473–489, <https://doi.org/10.1146/annurev.matsci.38.060407.132425>.
- [52] D. Quéré, Wetting and roughness, *Annu. Rev. Mater. Res.* 38 (2008) 71–99, <https://doi.org/10.1146/annurev.matsci.38.060407.132434>.
- [53] M. Jakob, W. Linke, Der Wärmeübergang von einer waagerechten Platte an siedendes Wasser, *Forsch. Auf Dem Gebiete Des Ingenieurwesens.* 4 (1933) 75–81, <https://doi.org/10.1007/BF02717048>.
- [54] L.M. Zysina-Molozhen, Some data on the number of centers of vaporization in boiling on industrial heating surfaces, *Probl. Heat Transf. Dur. A Chang. State a Collect. Artic*, 1953, pp. 155–159.
- [55] M. Trojer, R. Azizian, J. Paras, T. McKrell, K. Atkhen, M. Bucci, J. Buongiorno, A margin missed: the effect of surface oxidation on CHF enhancement in IVR accident scenarios, *Nucl. Eng. Des.* 335 (2018) 140–150, <https://doi.org/10.1016/j.nucengdes.2018.05.011>.
- [56] N. Zuber, Hydrodynamic Aspects of Boiling Heat Transfer, (1959), <https://doi.org/10.2172/4175511>.

Supplementary Data

Surface chemistry and morphology transition induced by critical heat flux incipience on laser- textured copper surfaces

Matic Može^{1,*}, Matevž Zupančič¹, Matej Hočevar², Iztok Golobič¹, Peter Gregorčič^{1,*}

¹*Faculty of Mechanical Engineering, University of Ljubljana, Aškerčeva 6, 1000 Ljubljana, Slovenia*

²*Institute of Metals and Technology, Lepi pot 11, 1000 Ljubljana, Slovenia*

Corresponding authors:

* *E-mail: matic.moze@fs.uni-lj.si (M. Može)*

* *E-mail: peter.gregorcic@fs.uni-lj.si (P. Gregorčič)*

Table of Contents

1. Microcavities on laser-textured surfaces

Figure S1. SEM images of laser-textured surfaces confirming the presence of multiscale microcavities on surfaces (a) L1 and (b) L2.

2. Surface roughness measurements

Table S1. Topographical characteristics of structured surfaces.

3. Validation of the dynamic measurement approach

Figure S2. Validation of dynamic boiling heat transfer performance measurement.

4. Low magnification SEM images of surfaces

Figure S3. Low magnification SEM images of laser-textured surface L1.

Figure S4. Low magnification SEM images of laser-textured surface L2.

5. High magnification SEM images of surfaces before and after boiling

Figure S5. High magnification SEM images of untreated reference surface REF before boiling.

Figure S6. High magnification SEM images of untreated reference surface REF after boiling.

Figure S7. High magnification SEM images of laser-textured surface L1 before boiling.

Figure S8. High magnification SEM images of laser-textured surface L1 after boiling.

Figure S9. High magnification SEM images of laser-textured surface L2 before boiling.

Figure S10. High magnification SEM images of laser-textured surface L2 after boiling.

6. AES analysis of surface atomic composition

Table S2. Results of the AES analysis of surface atomic composition.

Figure S11. Graphical presentation of the AES-analysis results of the surface atomic composition.

7. EDS analysis of surface atomic composition

Table S3. EDS analysis of surface atomic composition using 20 kV acceleration voltage.

Table S4. EDS analysis of surface atomic composition using 5 kV acceleration voltage.

Figure S12. Results of the EDS analysis (performed on surface REF) using two distinct excitation voltages before and after boiling.

Figure S13. Results of the EDS analysis (performed on surface L1) using two distinct excitation voltages before and after boiling.

Figure S14. Results of the EDS analysis (performed on surface L2) using two distinct excitation voltages before and after boiling.

8. XPS analysis of surface chemical composition

Table S5. Results of the XPS analysis of surface chemical composition – deconvolution of the C 1s peak.

Table S6. Results of the XPS analysis of surface chemical composition. The results are obtained by equation (1) from the main text as well as by the deconvolution of the Cu 2p_{3/2} peak and its shake-up satellite (fit of the curves).

Figure S15. C 1s peak on surface REF (a) before and (b) after boiling.

Figure S16. C 1s peak on surface L2 (a) before and (b) after boiling.

Figure S17. Cu 2p_{3/2} peak and its shake-up satellite on surface REF (a) before and (b) after boiling.

Figure S18. Cu 2p_{3/2} peak and its shake-up satellite on surface L2 (a) before and (b) after boiling.

9. Additional experiment with replaced water

Figure S19. Boiling curves recorded during additional experiments aimed at excluding the influence of water contamination on the measurement results.

1 Microcavities on laser-textured surfaces

Multiscale microcavities were deliberately created using specific laser-texturing parameters. As explained in the main text, these cavities mainly form where melted and resolidified material from adjacent laser beam traces overlaps. Red and blue circles in Figure 1 denote microcavities on the aforementioned ridge of resolidified material. It is noticeable that the microcavities are (i) in the micrometer size range and (ii) span across multiple length scales. The measured diameters of microcavities are in the range of 0.35-5.6 μm for surface L1 and 0.37-4.9 μm for surface L2.

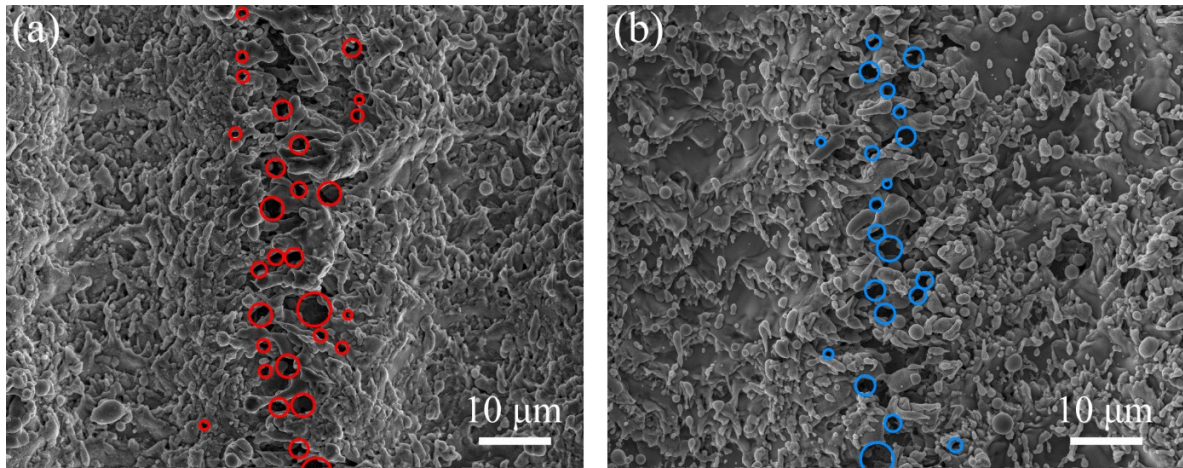


Figure S1. SEM images of laser-textured surfaces confirming the presence of multiscale microcavities on surfaces (a) L1 and (b) L2.

2 Surface roughness measurements

Roughness of every surface was recorded using an Alicona InfiniteFocusSL microscope with a 20x magnification lens. The results of roughness analysis are listed in Table S1. A patch of 3x3 mm² was analyzed on every surface to record the *Sa* value. For anisotropic surfaces, *Ra* was also recorded.

Table S1. Topographical characteristics of structured surfaces.

Sample	Treatment	<i>Sa</i> (μm)	<i>Ra</i> (μm)	Comment
REF	mechanical (sanding with P2000 grit)	0.15	/*	*isotropic surface
L1	laser texturing (microcavities produced in air)	3.01	2.98*	*perpendicular to the grooves
L2	laser texturing (microcavities produced in argon)	2.15	2.14*	*perpendicular to the grooves

3 Validation of the dynamic measurement approach

Measurements were performed using a dynamic measurement method where the heat flux was slowly but continuously increased by increasing the voltage supplied to the cartridge heaters in the heating block. This has the potential to cause deviations from true and accurate results due to thermal capacitance of the system (especially the heating block). Consequently, a validation experiment was performed to compare experimental results of steady state and dynamic measurements. A total of four successive dynamic measurements were performed to record four boiling curves. An additional experimental run followed where the system was left to stabilize at 5 distinct cartridge heater powers. After a steady state was reached, the results were collected and averaged for 10 minutes. As it is evident from Figure S2, the steady state measurement points do not differ from the boiling curves recorded using a dynamic approach; any deviations are well within the measurement uncertainty.

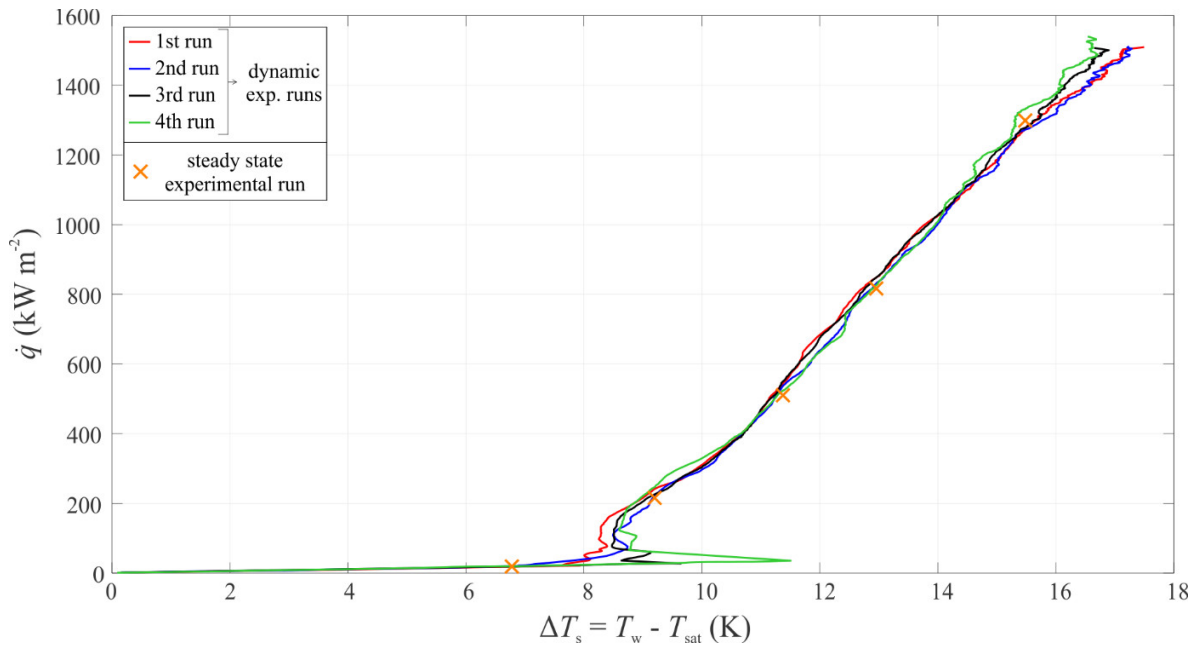


Figure S2. Validation of dynamic boiling heat transfer performance measurement.

4 Low magnification SEM images of surfaces

Low magnification SEM images of surfaces are shown in Figures S3 and S4. Images were recorded using a JEOL JSM-6500F scanning electron microscope.

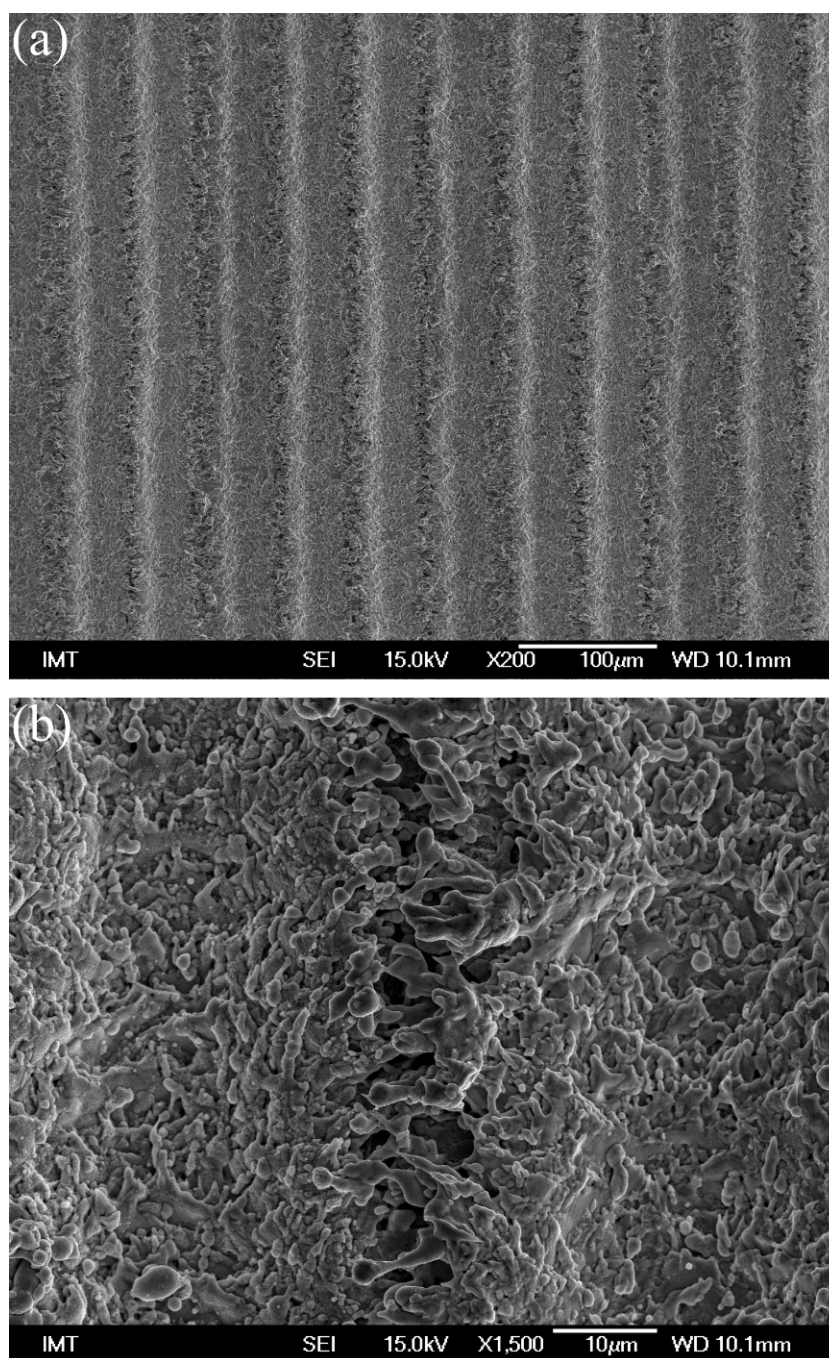


Figure S3. Low magnification SEM images of laser-textured surface L1.

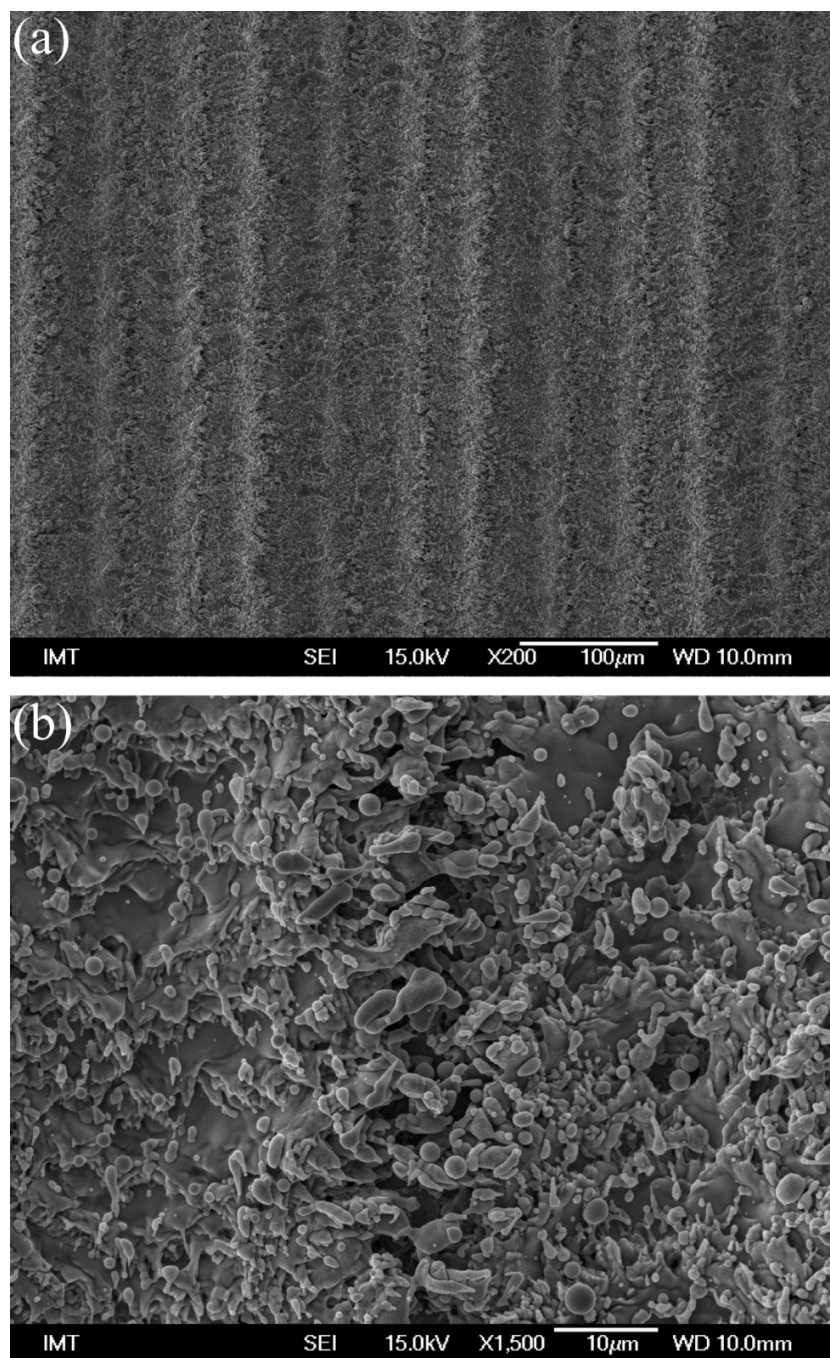


Figure S4. Low magnification SEM images of laser-textured surface L2.

5 High magnification SEM images of surfaces before and after boiling

High magnification SEM images of several laser-textured surfaces are shown in Figures S5-S10. Images were recorded using a JEOL JSM-6500F scanning electron microscope.

5.1 Surface “REF”

Figure S5 shows high magnification SEM images of the untreated reference surface before boiling experiments, while the high magnification SEM images of the same surface after boiling experiments are shown in Figure S6.

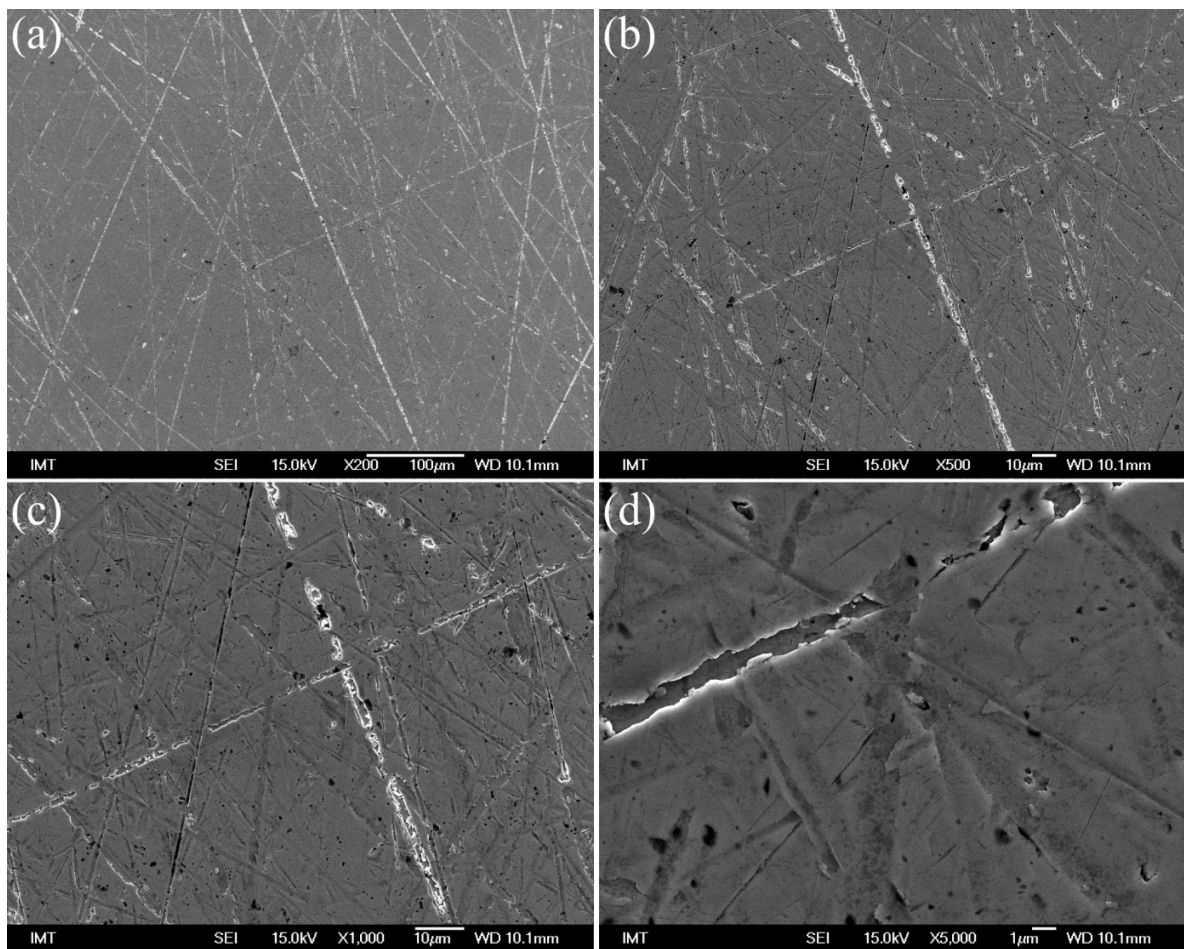


Figure S5. High magnification SEM images of untreated reference surface REF before boiling.

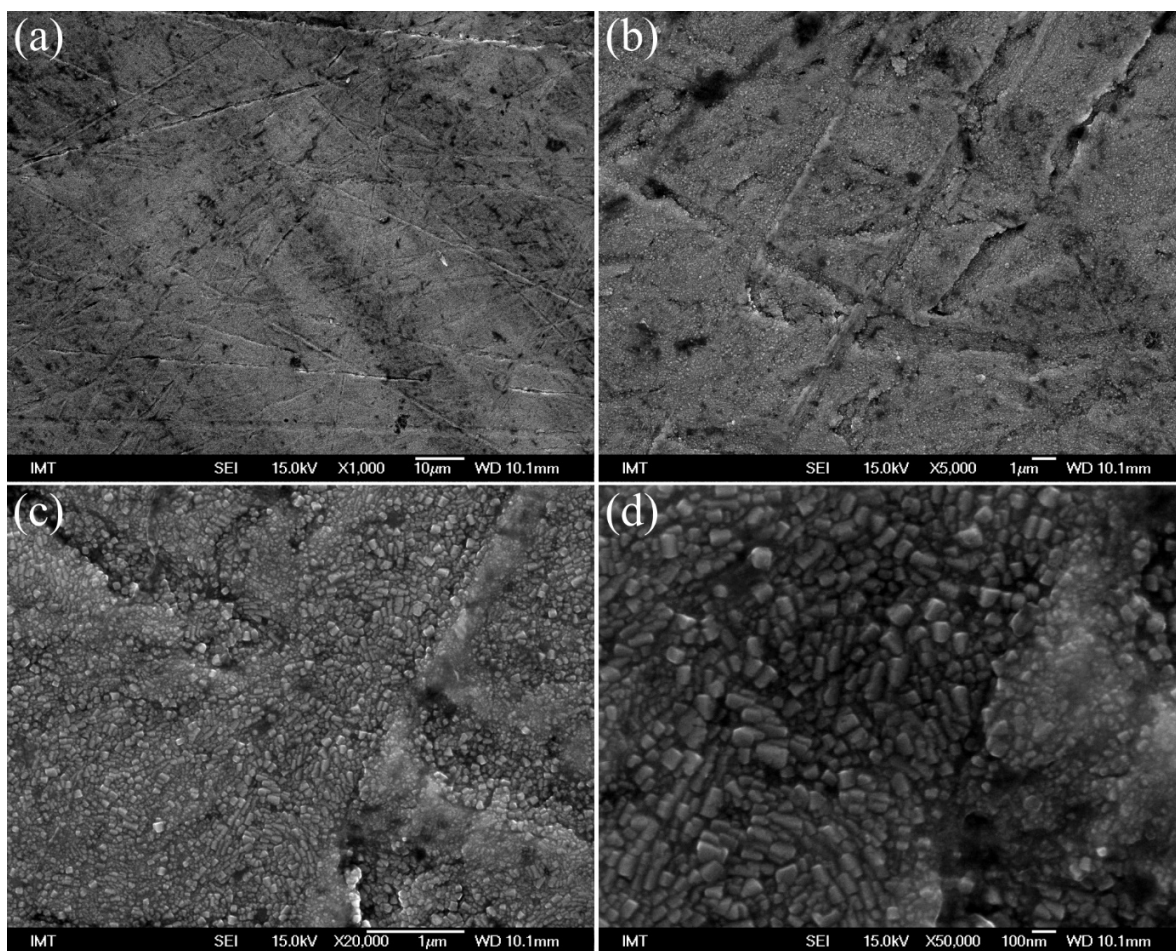


Figure S6. High magnification SEM images of untreated reference surface REF after boiling.

5.2 Surface “L1”

Figure S7 shows high magnification SEM images of the laser-textured surface L1 (in air atmosphere) before boiling experiments, while the same surface after boiling experiments is shown in Figure S8. A change in morphology is clearly noticeable.

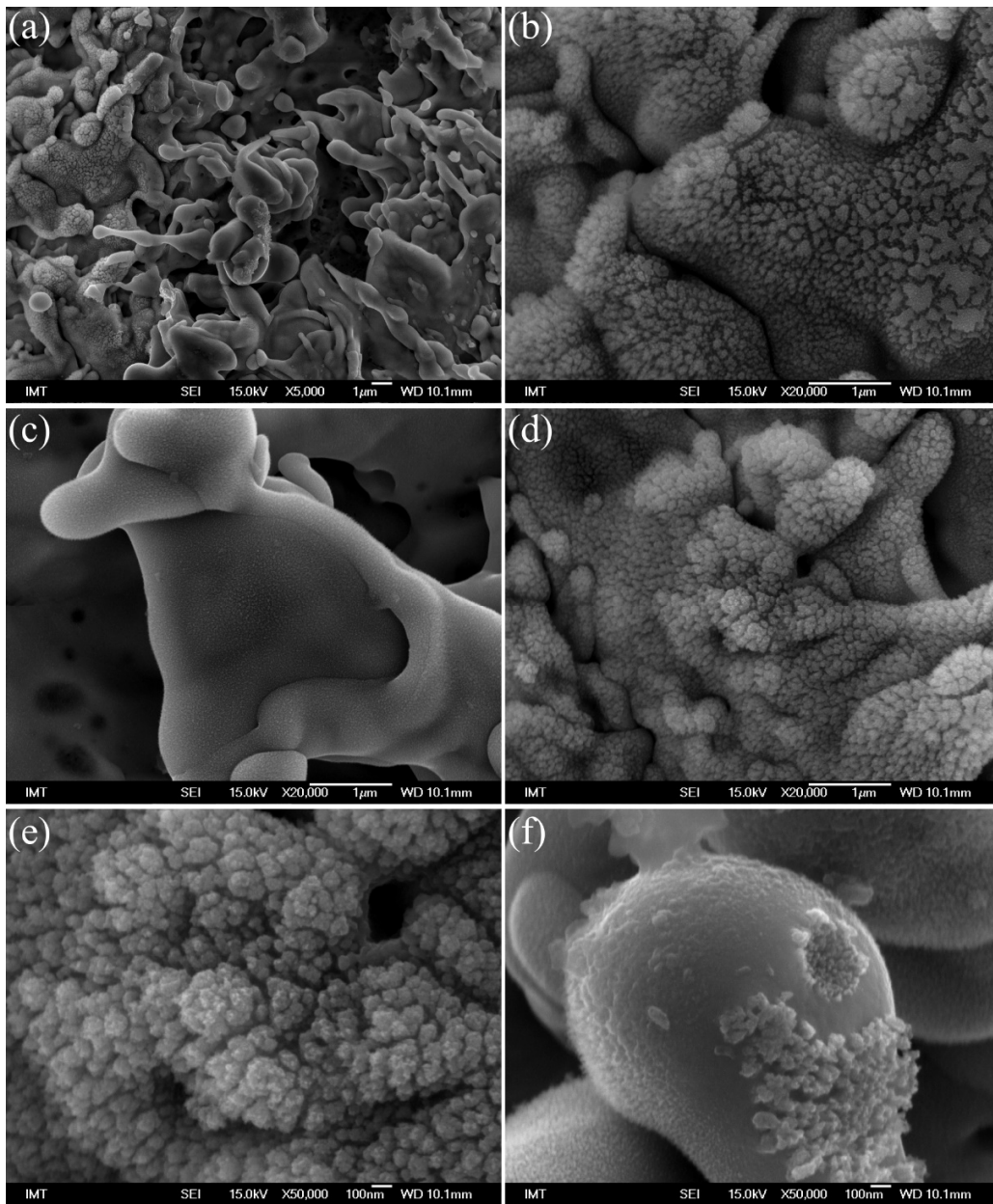


Figure S7. High magnification SEM images of laser-textured surface L1 before boiling.

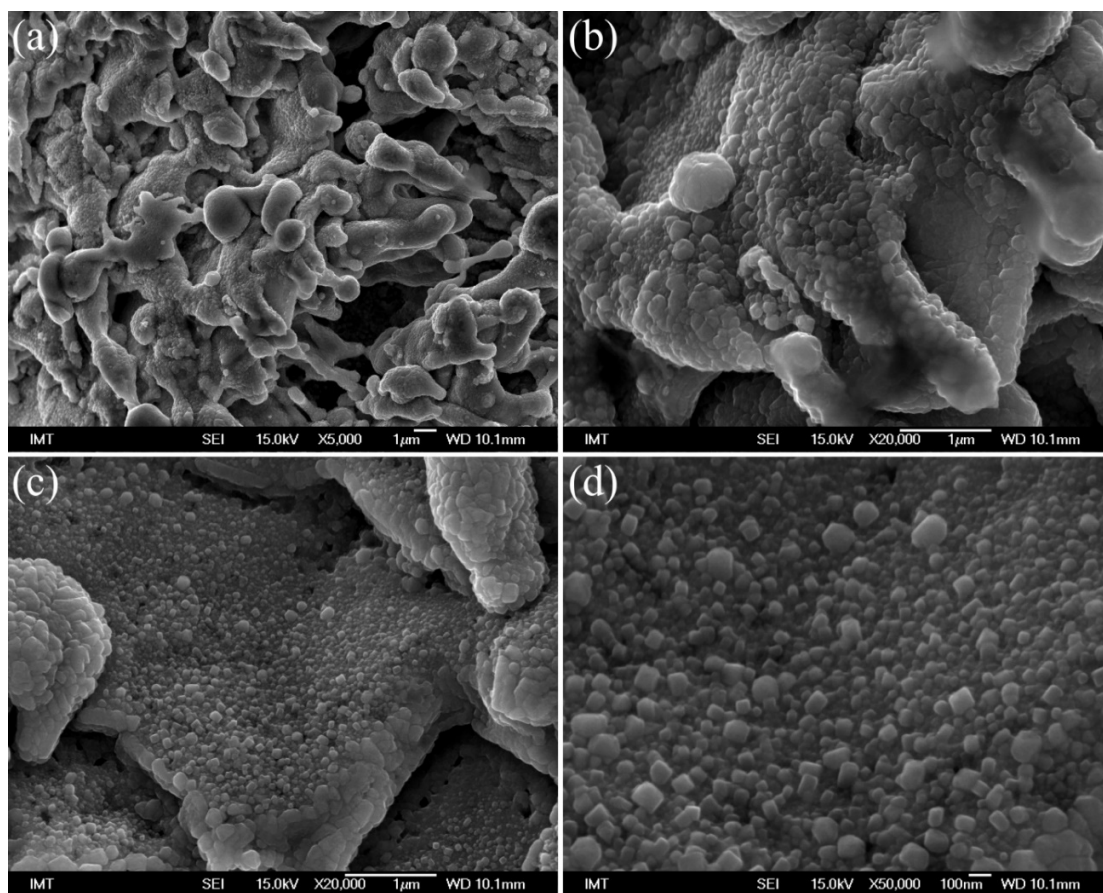


Figure S8. High magnification SEM images of laser-textured surface L1 after boiling.

5.2.1 Surface “L2”

Figure S9 shows high magnification SEM images of the laser-textured surface L2 (in argon atmosphere) before boiling experiments, while the same surface after boiling experiments is shown in Figure S10. Here, the morphology changes are less pronounced as on the surface L1.

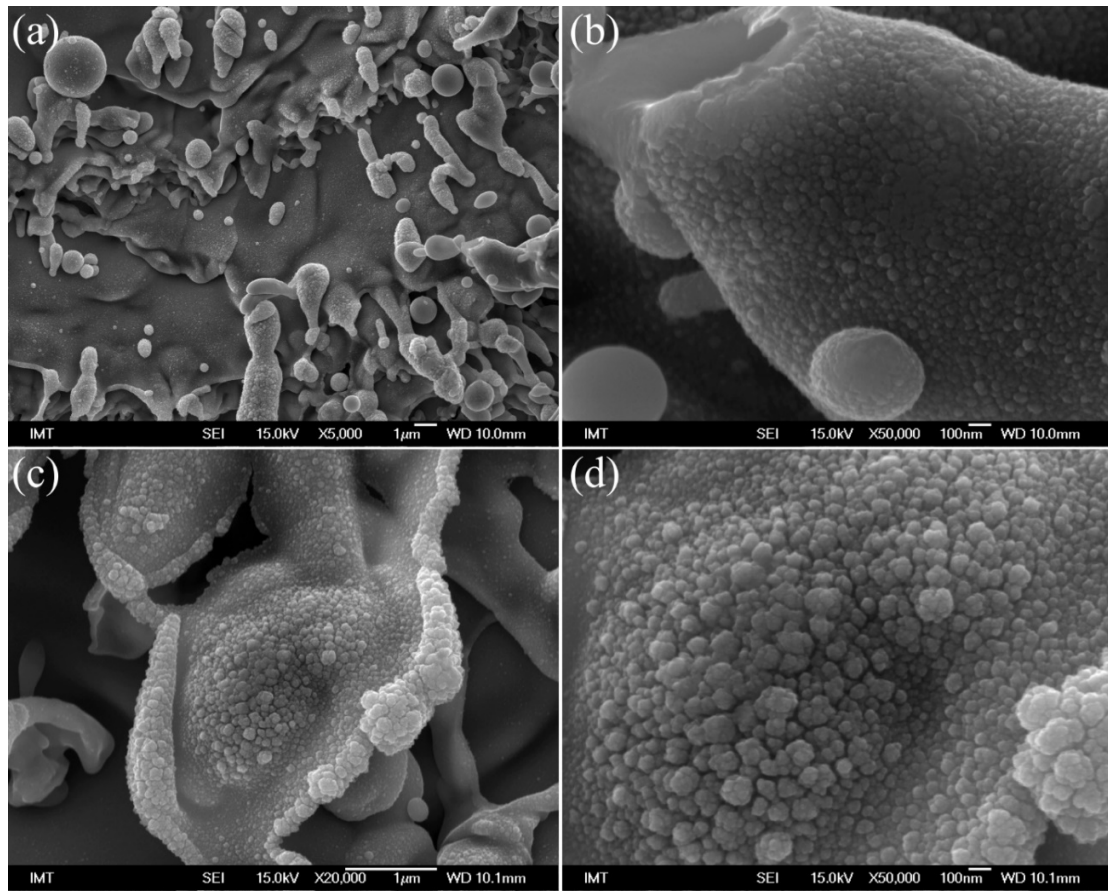


Figure S9. High magnification SEM images of laser-textured surface L2 before boiling.

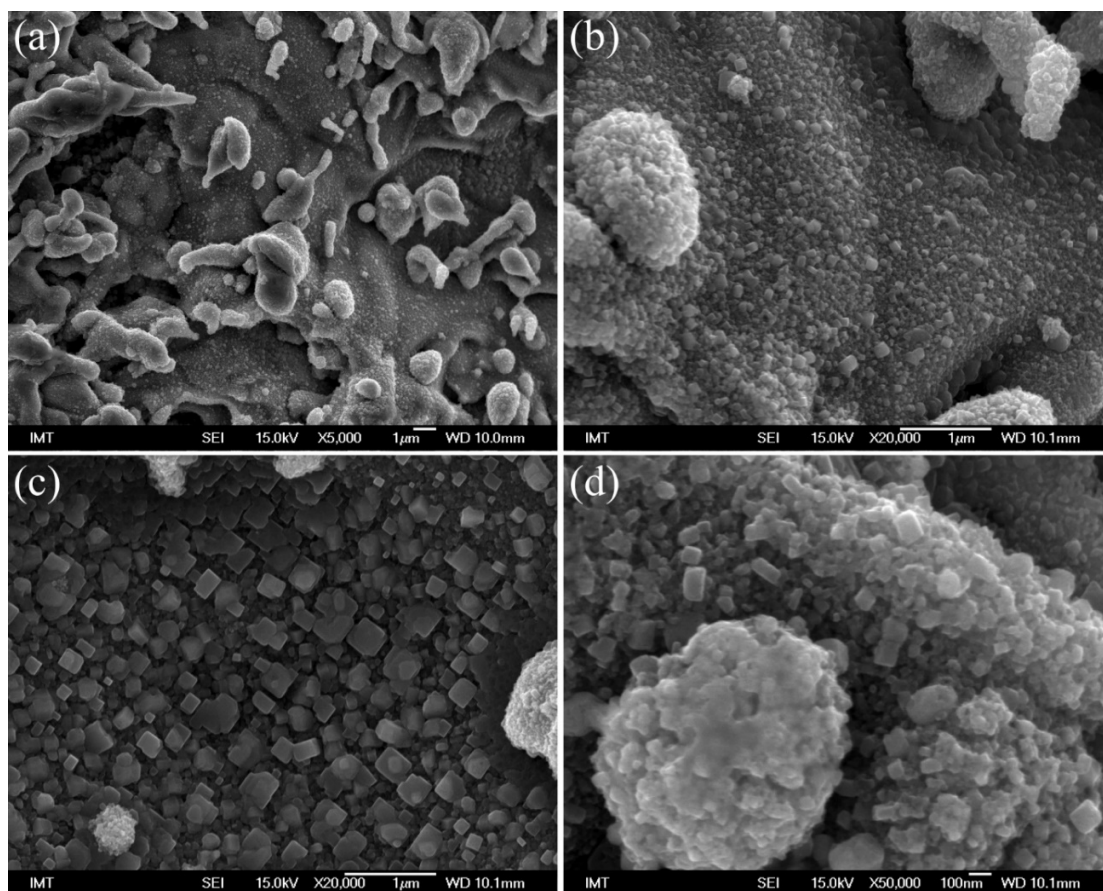


Figure S10. High magnification SEM images of laser-textured surface L2 after boiling.

6 AES analysis of surface atomic composition

Table S2. Results of the AES analysis of surface atomic composition.

Sample	Point of measurement	at. % C	at. % O	at. % Cu	at. % N	O/Cu ratio
REF	before boiling	73.3	11.2	15.6	0	0.72
	after boiling	68.8	21.1	10.2	0	2.07
L1	before boiling	32.5	42.0	25.5	0	1.65
	after boiling	46.5	28.4	20.6	4.6	1.38
L2	before boiling	33.8	32.2	34.0	0	0.95
	after boiling	44	20.4	26.5	9.2	0.77

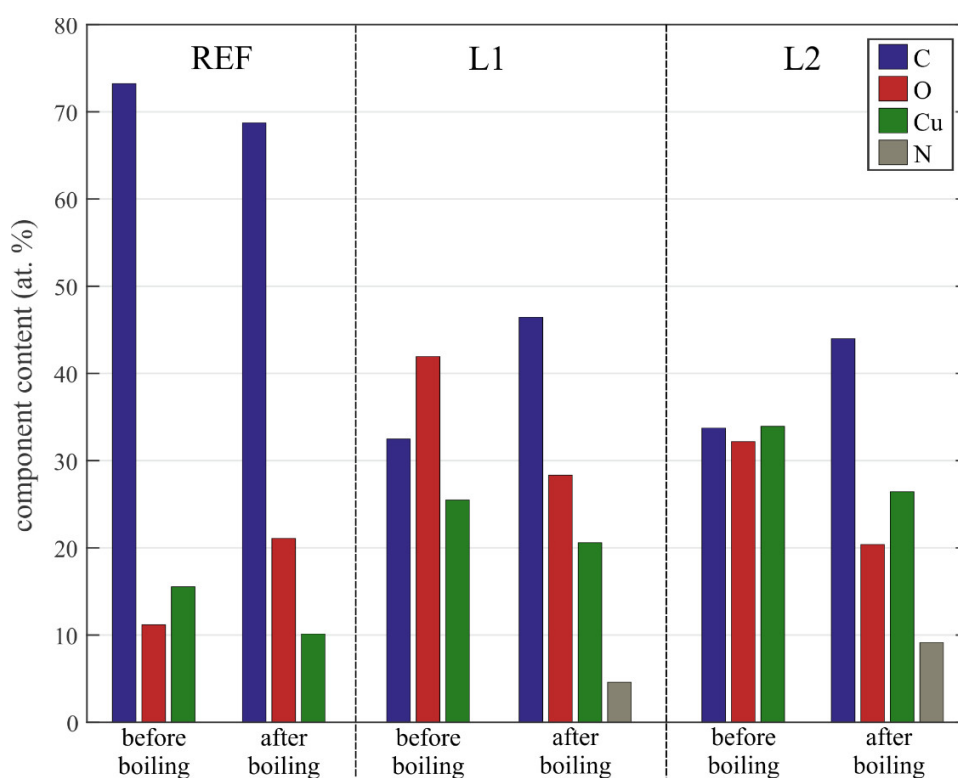


Figure S11. Graphical presentation of the AES-analysis results of the surface atomic composition.

7 EDS analysis of surface atomic composition

EDS analysis was conducted at two different acceleration voltages. The results are listed in Tables S3 and S4; they are also shown in Figures S12-S14.

Table S3. EDS analysis of surface atomic composition using 20 kV acceleration voltage.

Sample	Point of measurement	at. % C	at. % O	at. % Cu	O/Cu ratio
REF	before boiling	12.21	3.61	84.17	0.04
	after boiling	23.57	6.8	69.63	0.10
L1	before boiling	18.98	19.01	62.01	0.31
	after boiling	12.81	13.07	74.12	0.18
L2	before boiling	13.61	5.22	81.17	0.06
	after boiling	12.33	12.51	75.16	0.17

Table S4. EDS analysis of surface atomic composition using 5 kV acceleration voltage.

Sample	Point of measurement	at. % C	at. % O	at. % Cu	O/Cu ratio
REF	before boiling	8.34	5.09	86.56	0.06
	after boiling	18.16	16.89	64.94	0.26
L1	before boiling	15.81	35.55	48.64	0.73
	after boiling	10.77	22.71	66.52	0.34
L2	before boiling	10.93	10.37	78.69	0.13
	after boiling	11.65	21.57	66.79	0.32

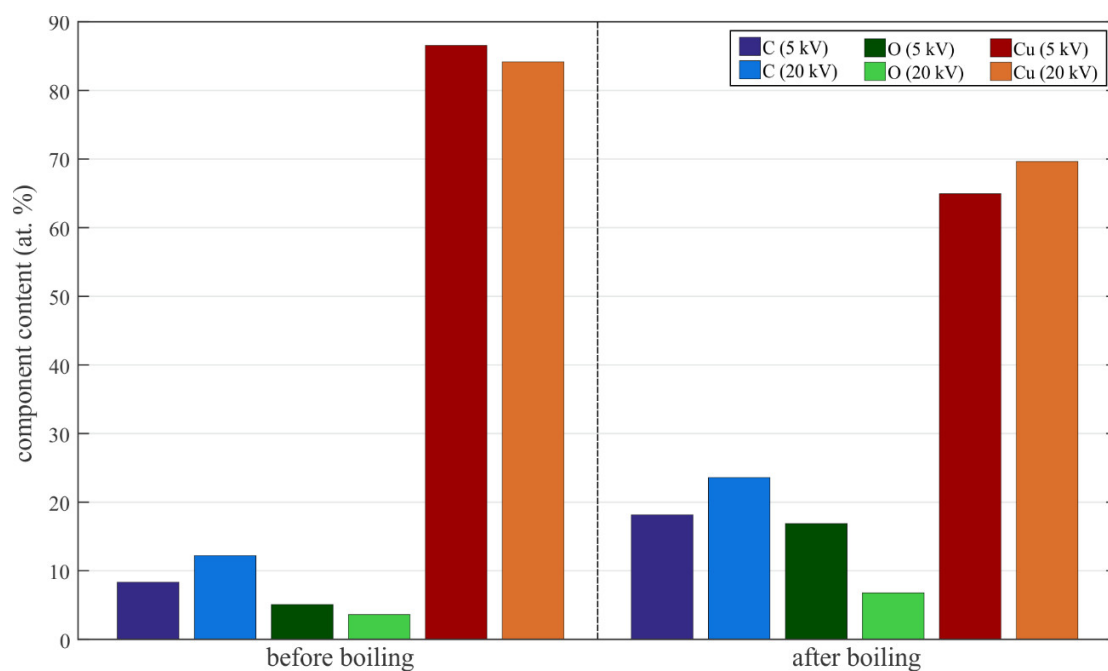


Figure S12. Results of the EDS analysis (performed on surface REF) using two distinct excitation voltages before and after boiling.

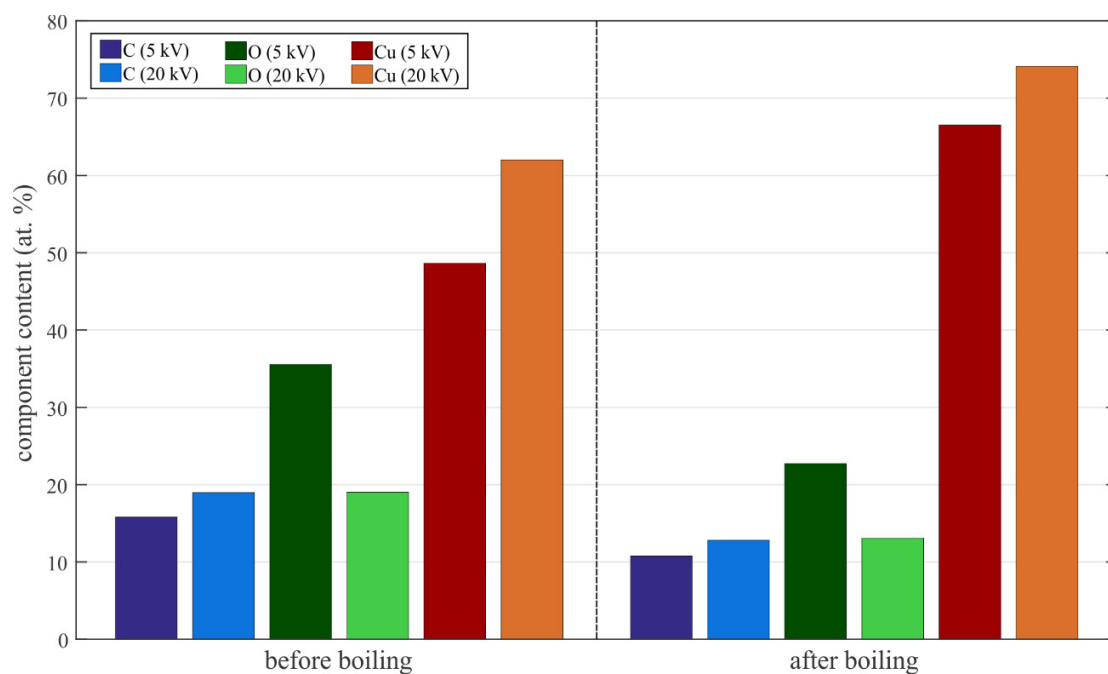


Figure S13. Results of the EDS analysis (performed on surface L1) using two distinct excitation voltages before and after boiling.

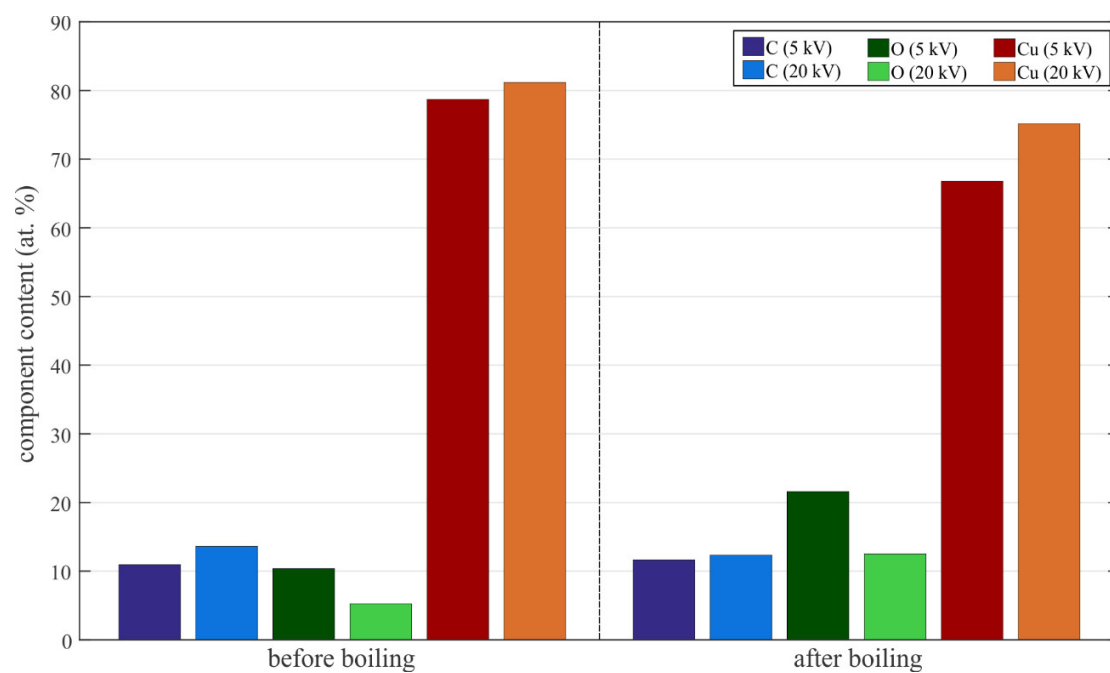


Figure S14. Results of the EDS analysis (performed on surface L2) using two distinct excitation voltages before and after boiling.

8 XPS analysis of surface chemical composition

XPS analysis included fitting the components of C 1s peak. The fitted parameters are summarized in Table S5. As described in the main text, the Cu/Cu₂O ratio was estimated from the Cu 2p_{3/2} peak by measuring the areas of the main peak and its shake-up satellite [see the equation (1) in the main text] as well as by using appropriate peak deconvolution. The results are summarized in Table S6. It clearly follows that the results, obtained from the areas under the main and the shake-up satellite peaks conforms well with the results from the fit of the XPS signal.

The narrow scans and deconvolutions of the C 1s peaks are shown in Figures S15-S16 for samples REF and L2 before and after boiling experiments, while the narrow scans of the Cu 2p_{3/2} peaks for the same samples are shown in Figures S17 and S18. Here, the area of the main peak is colored blue, while the red color is used for its shake-up satellite.

Table S5. Results of the XPS analysis of surface chemical composition – deconvolution of the C 1s peak.

Sample	Point of meas.	C-C, C-H			C-O			O-C=O		
		BE (eV)	FWHM (eV)	at. %	Δ BE from C-C (eV)	FWHM (eV)	at. %	Δ BE from C-C (eV)	FWHM (eV)	at. %
REF	before boiling	284.7	2.05	79.9	1.6	2.15	11.9	3.6	2.25	8.2
	after boiling	284.7	1.67	83.6	1.6	1.77	12.0	3.6	1.87	4.4
L1	before boiling	284.7	1.78	58.7	1.4	1.88	19.4	3.75	2.03	21.9
	after boiling	284.7	1.77	71.5	1.5	1.87	19.0	3.55	1.97	9.4
L2	before boiling	284.7	1.66	62.9	1.4	1.76	20.6	3.65	1.86	16.6
	after boiling	284.7	1.76	48.7	1.5	1.84	34.2	3.4	1.94	17.1

Table S6. Results of the XPS analysis of surface chemical composition. The results are obtained by equation (1) from the main text as well as by the deconvolution of the Cu 2p_{3/2} peak and its shake-up satellite (fit of the XPS signal).

Sample	Point of measurement	using eq. (1)	fit of the XPS signal		
		at. % Cu/Cu ₂ O	at. % Cu/Cu ₂ O	at. % CuO	at. % Cu(OH) ₂
REF	before boiling	80-83	81	2	17
	after boiling	82-84	82	15	3
L1	before boiling	11-21	16	27	57
	after boiling	86-88	87	12	1
L2	before boiling	65-69	67	21	11
	after boiling	70-73	70	20	10

8.1 XPS – C 1s peak

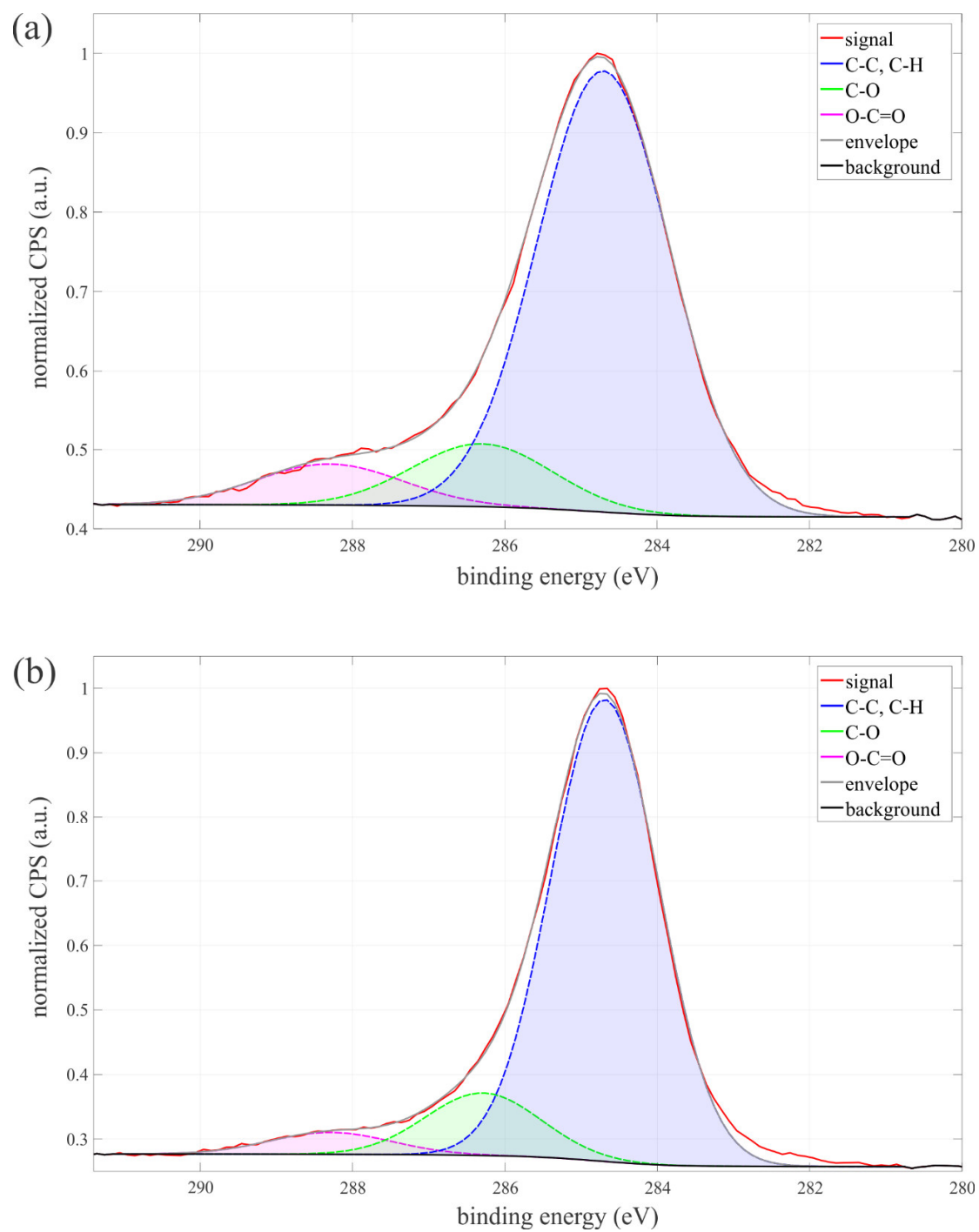


Figure S15. C 1s peak on surface REF (a) before and (b) after boiling.

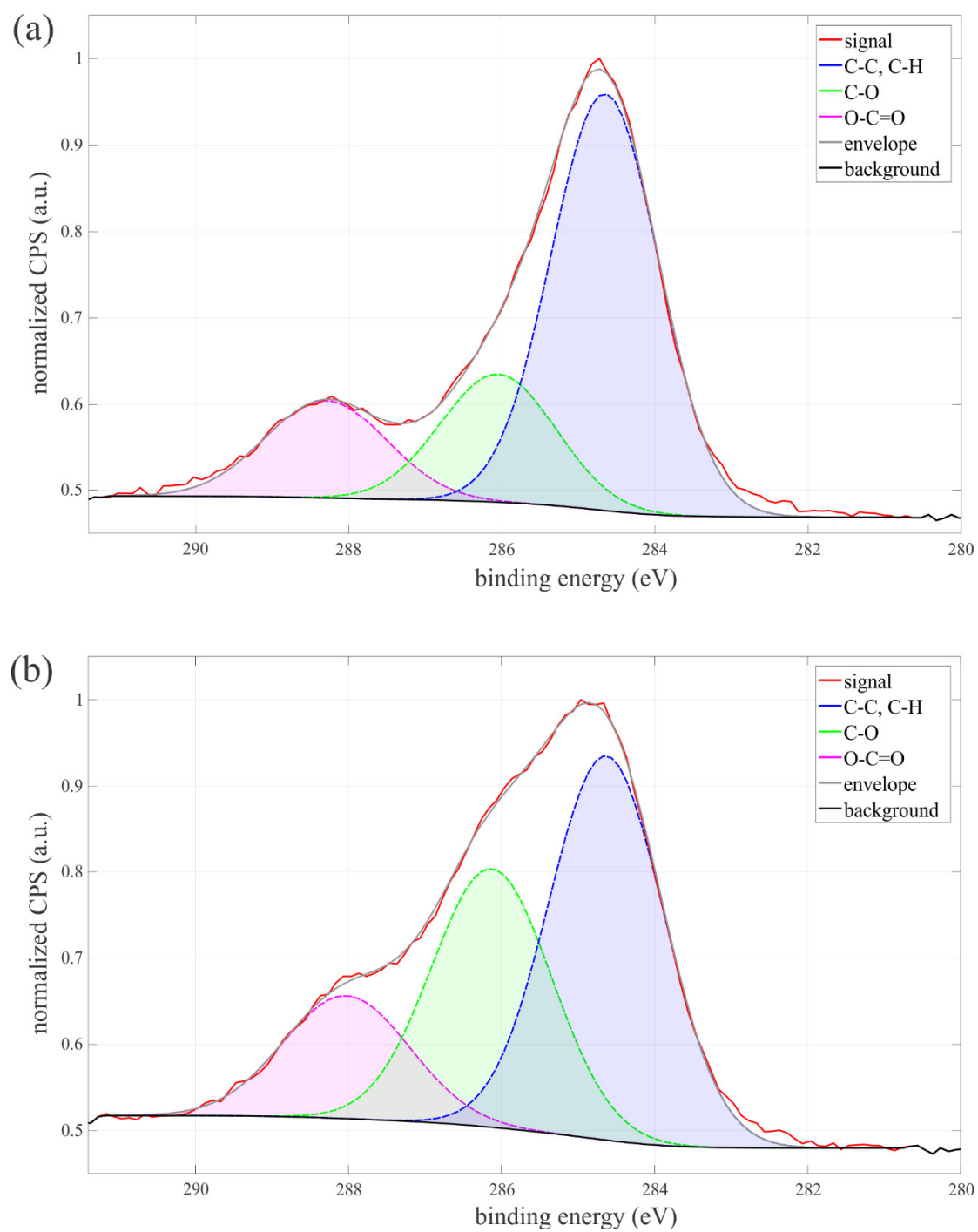


Figure S16. C 1s peak on surface L2 (a) before and (b) after boiling.

8.2 XPS – Cu 2p_{3/2} peak and its shake-up satellite

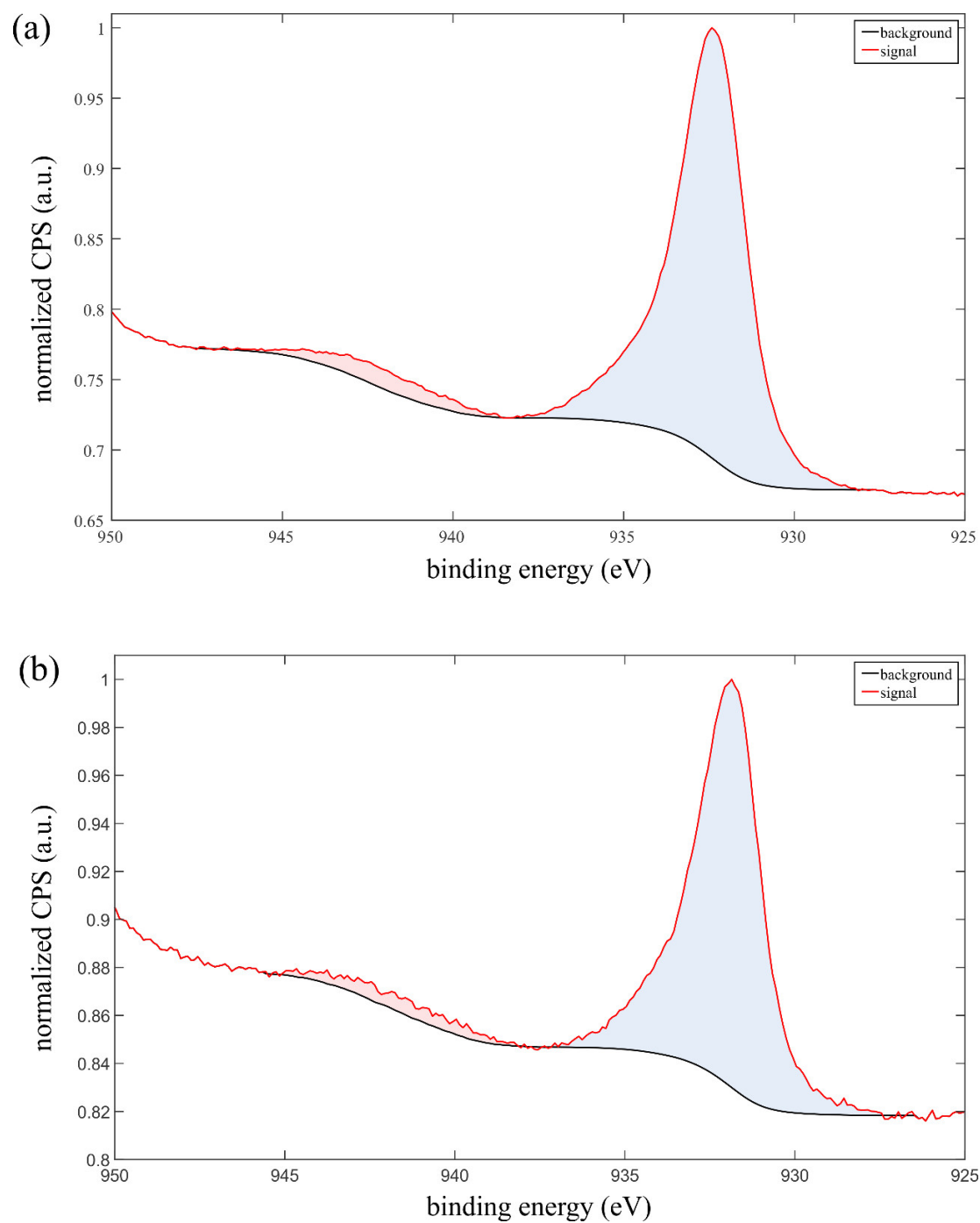


Figure S17. Cu 2p_{3/2} peak and its shake-up satellite on surface REF (a) before and (b) after boiling.

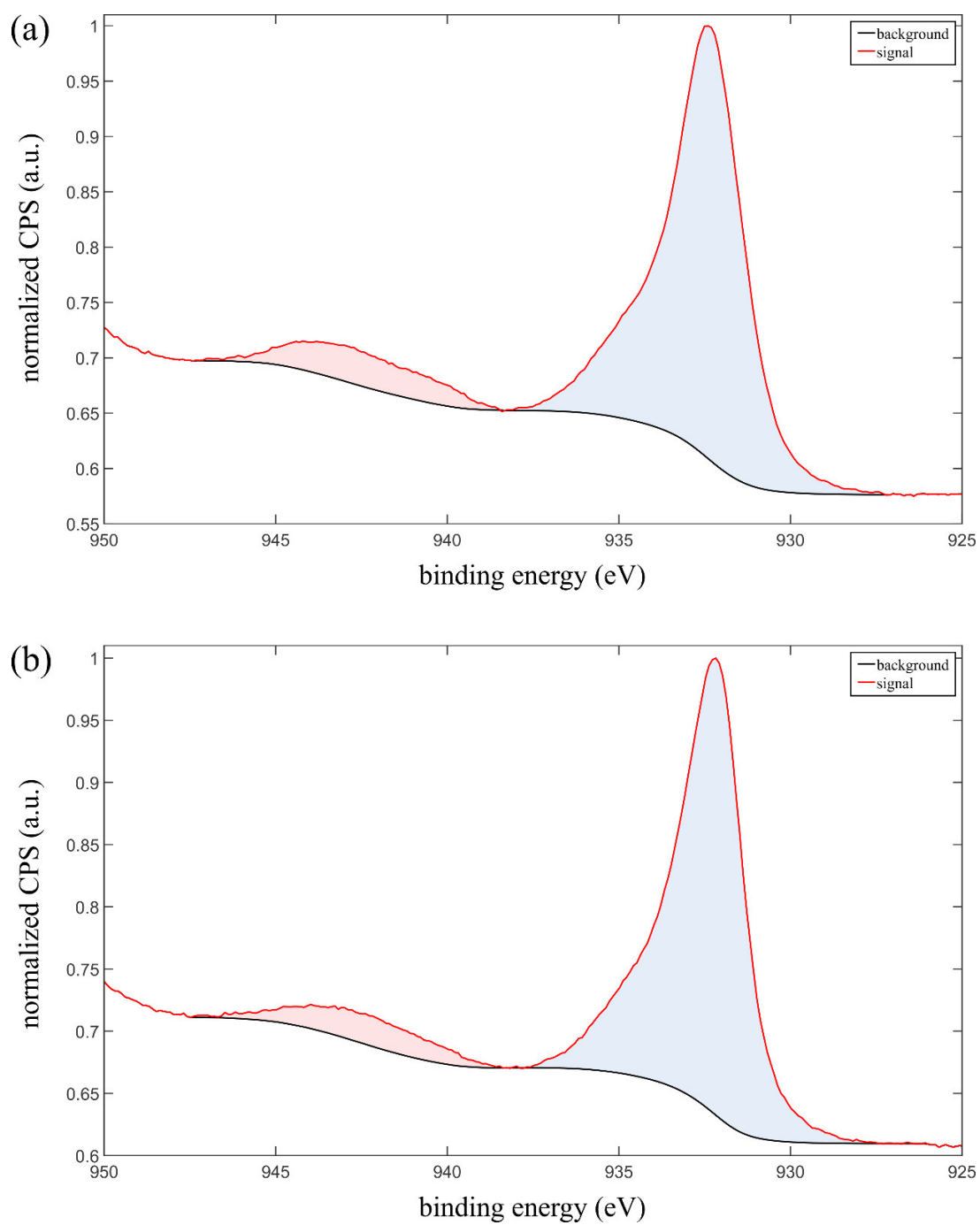


Figure S18. Cu 2p_{3/2} peak and its shake-up satellite on surface L2 (a) before and (b) after boiling.

9 Additional experiment with replaced water

The results of the additional experiment aimed at excluding the possible influence of water on the boiling curve shift are shown in Figure S19. The experiment was carried out on a thermally oxidized smooth copper surface. The surface was not a part of this research project but displays the noted boiling curve shift regardless. The measurements were conducted in accordance with the protocol described in main text. CHF was reached during the first measurement and again during the second experimental run. After the water cooled down, it was replaced with fresh water; attention was paid so that the still hot boiling surface did not come into contact with air while the water was being replaced. Two more experimental runs were conducted with CHF being reached during both. Should the leakage of substance into the water or some other change in its chemistry be responsible for the boiling curve shift, the boiling curves should gravitate towards the original (first) boiling curve after the water was replaced. As this did not happen, it can be assumed that no significant changes happened to the working fluid as a consequence of high temperature being reached during CHF events. Therefore, the boiling curve shift must be a consequence of changes in surface chemistry and/or surface topography.

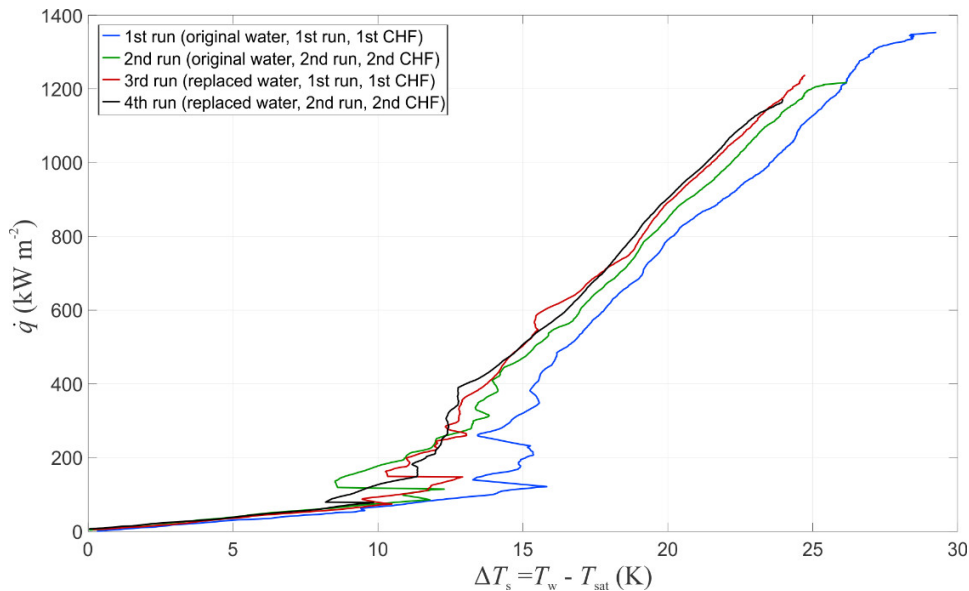


Figure S19. Boiling curves recorded during additional experiments aimed at excluding the influence of water contamination on the measurement results.